Kinematics of chromodynamic multicomponent lattice Boltzmann simulation with a large density contrast

K. Burgin,[1] J. Spendlove,[1] X. Xu,[1,2] and I. Halliday[1,*]

[1]*Materials & Engineering Research Institute, Sheffield Hallam University, Howard Street, S1 1WB, United Kingdom*

[2]*Department of Engineering and Mathematics, Sheffield Hallam University, Howard Street, S1 1WB, United Kingdom*

(Received 24 April 2019; published 31 October 2019)

The utility of an enhanced chromodynamic, color gradient or phase-field multicomponent lattice Boltzmann (MCLB) equation for immiscible fluids with a density difference was demonstrated by Wen *et al.* [Phys. Rev. E **100**, 023301 (2019)] and Ba *et al.* [Phys. Rev. E **94**, 023310 (2016)], who advanced earlier work by Liu *et al.* [Phys. Rev. E **85**, 046309 (2012)] by removing certain error terms in the momentum equations. But while these models' collision scheme has been carefully enhanced by degrees, there is, currently, no quantitative consideration in the macroscopic dynamics of the segregation scheme which is common to all. Here, by analysis of the kinetic-scale segregation rule (previously neglected when considering the continuum behavior) we derive, bound, and test the emergent kinematics of the continuum fluids' interface for this class of MCLB, concurrently demonstrating the circular relationship with—and competition between—the models' dynamics and kinematics. The analytical and numerical results we present in Sec. V confirm that, at the kinetic scale, for a range of density contrast, color is a material invariant. That is, within numerical error, the emergent interface structure is isotropic (i.e., without orientation dependence) and Galilean-invariant (i.e., without dependence on direction of motion). Numerical data further suggest that reported restrictions on the achievable density contrast in rapid flow, using chromodynamic MCLB, originate in the effect on the model's kinematics of the terms deriving from our term F_{1i} in the evolution equation, which correct its dynamics for large density differences. Taken with Ba's applications and validations, this result significantly enhances the theoretical foundation of this MCLB variant, bringing it somewhat belatedly further into line with the schemes of Inamuro *et al.* [J. Comput. Phys. **198**, 628 (2004)] and the free-energy scheme [see, e.g., Phys. Rev. E. **76**, 045702(R) (2007), and references therein] which, in contradistinction to the present scheme and perhaps wisely, postulate appropriate kinematics *a priori*.

DOI: 10.1103/PhysRevE.100.043310

I. INTRODUCTION

Since 1991, when Gunstensen and Rothman [1] devised the essential technique, several forms of multicomponent lattice Boltzmann (MCLB) equation methods have been developed to address issues of application regime (i.e., physical content), algorithmic stability, and accuracy. The current method which most closely resembles Gunstensen's is the *chromodynamic* variant. While chromodynamic MCLB is based upon minimal physics (flow mechanics and continuum interfacial boundary conditions), it overcomes the original limitations of Gunstensen's method (a lack of Galilean invariance, drop faceting, lattice pinning and a large interfacial microcurrent), which nevertheless remains a benchmark of statistical physics, with its roots in the highly novel immiscible lattice gas (ILG). For a full discussion, see Ref. [2] or Rothman and Zaleski's remarkable 1997 book [3]. The present article is concerned with chromodynamic MCLB isothermal, completely immiscible fluids with a density difference.

Other MCLB variants represent more substantial extensions to the ILG, not least because they are adapted to multiphase *and* multicomponent flow simulation. Like the chromodynamic variant, they contain flow mechanics (i.e., Navier-Stokes and continuity equations) and are conveniently classified by additional physics embedded in their fluid-fluid interface algorithm. Where the kinetics of phase separation are important, *free-energy* methods [4,5] and their thermodynamically consistent extensions, due to Wagner and coworkers [6–8], based, as they are, on the Cahn-Hilliard theory, are appropriate. For workers with a background in molecular simulation, the *Shan-Chen* method [9] is the natural and, possibly, most popular choice for applications requiring an ability to simulate large density contrasts up to 800, between components or phases, albeit with an increased interfacial width, and reduced viscosity contrast [10]. See also the method of Innamuro *et al.* [11]. Meanwhile, the free-energy method is, arguably, the most physically complete MCLB. In addition to thermodynamic consistency, it is important to note that it employs an order parameter to distinguish fluids, which has convection-diffusion dynamics *a priori*. The present article seeks to confirm equivalent behavior (which amounts to an effective kinematic condition) in the chromodynamic MCLB variant.

In continuum isothermal hydrodynamics, multicomponent flow is defined by the Navier-Stokes and continuity equations together with the dynamic and kinematic conditions at the interface [12]. In this regime, it is safe to employ the

*Corresponding author: i.halliday@shu.ac.uk

chromodynamic method, since here its lack of a thermodynamic foundation is not an impediment. The enhanced foundation for chromodynamic MCLB we set out will increase researchers' confidence with this minimal, computationally straightforward method, applied to this regime, where the free-energy method also works well [10].

For present purposes, the chromodynamic method is taken to be a combination of the algorithms of Lishchuk *et al.* [13] and d'Ortona *et al.* [14]. To induce interfacial tension, chromodynamic MCLB uses an immersed boundary force [15] with Galilean invariant performance (if velocity corrections are applied [16]) and a computationally efficient, analytic component segregation [14]. Previously identified limitations notwithstanding, the method transparently encapsulates Laplacian interfacial tension and a no-traction condition [13], has a low microcurrent and interface width, can address large viscosity contrasts, and it allows direct parametrization of interfacial tension [17]. We note, here, that Reiss and Phillips [18] developed computationally efficient interfacial perturbation operators in place of the Lishchuk force which, arguably, offer the most physically consistent encapsulation of interfacial tension in a distribution function-based technique, such as MCLB.

A common factor in continuum MCLB applications to the continuum scale is that an interface should be subject to a kinematic condition, i.e., advect at the same speed as the embedding fluid. It is important that MCLB variants may be shown to contain such a condition—especially where its absence might lead to computational instability. To answer this need, one must either embed the condition explicitly (as in the free-energy method; see also Innamuro *et al.* [11]) or proceed as we do here—project the relevant physics from the kinetic scale behavior (i.e., the computational algorithm) and then assess numerical data from that model to quantify and bound compliance. The first step is challenging because MCLB formulation lies within discrete kinetic theory, but it is the behavior of the continuum which must exhibit a kinematic condition.

The principal motives here are to show, by analysis of the segregation rule, the interplay between kinematics and dynamics in a large density difference (LDD) chromodynamic MCLB variant, derive its continuum scale kinematics, and, using computational data, quantify its applicability. To achieve this we interrelate analyses of segregation and collision schemes. Our results address the kinematics of the method, since the dynamics of LDD two-component MCLB methods of chromodynamic class, developed by Wen *et al.* [19], Ba *et al.* [20], Liu *et al.* [21] have already been benchmarked in the continuum regime applications [20]. These authors extend the segregation method of d'Ortona *et al.* [14] to LDD, but use a multirelaxation-time (MRT) collision scheme, which obscures the interaction between model kinematics and dynamics. To simplify, we develop a LDD lattice Boltzmann Bhatnagar-Gross-Krook (LBGK) collision scheme and recast these analyses to a "one-fluid" formulation, where a single set of equations describes the entire flow field. We organize as follows: In Sec. II we contextualise and present our one-fluid formulation. In Sec. III we demonstrate emergence of physically correct kinematics by analytical methods, assuming the LBGK model developed in Sec. IV. In Sec. V we verify our predictions of model kinematics and consider its extension to Ba's MRT scheme, and we present our conclusions in Sec. VI.

II. ONE-FLUID FORMULATION FOR LARGE DENSITY DIFFERENCE

To analyze the continuum-scale kinematics of a LDD interface, we express the implementation of the chromodynamic variant in a convenient, color-blind form. For two immiscible components designated red and blue, described by distribution functions $R_i(\mathbf{r}, t)$ and $B_i(\mathbf{r}, t)$, where

$$f_i(\mathbf{r}, t) = R_i(\mathbf{r}, t) + B_i(\mathbf{r}, t), \tag{1}$$

a two-component, scheme for LDD MCLB may be formulated as follows:

$$f_i(\mathbf{r} + \delta_t \mathbf{c}_i, t + \delta_t) = f_i(\mathbf{r}, t) - \frac{\delta_t}{\tau}\left[f_i(\mathbf{r}, t) - f_i^{(0)}(\rho, \mathbf{u})\right] + F_{1i} + F_{2i}, \tag{2}$$

where the density-difference supporting equilibrium, $f_i^{(0)}(\rho, \mathbf{u})$, redistributes mass away from the rest ($i = 0$) link via term ϕ_i (to be discussed shortly):

$$f_i^{(0)}(\rho, \mathbf{u}) = \rho\phi_i + t_i\rho\left(\frac{u_\alpha c_{i\alpha}}{c_s^2} + \frac{u_\alpha u_\beta c_{i\alpha} c_{i\beta}}{2c_s^4} - \frac{u^2}{2c_s^2}\right). \tag{3}$$

Evolution equation source terms which correct the dynamics in the presence of large density contrasts (see, e.g., Ref. [20]) and apply an immersed boundary or body force, $F_\alpha(\mathbf{r})$, $\alpha \in [x, y, z]$ are respectively F_{1i} and F_{2i}. A suitable correction F_{1i} remains to be determined however:

$$F_{2i} = \left(1 - \frac{1}{2\tau}\right)\left(\frac{F_\alpha(c_{i\alpha} - u_\alpha)}{c_s^2} + \frac{F_\alpha u_\beta c_{i\alpha} c_{i\beta}}{2c_s^4}\right). \tag{4}$$

Note that we assume that force-adjusted macroscopic observables are used:

$$\rho_R(\mathbf{r}, t) = \sum_i R_i(\mathbf{r}, t), \quad \rho_B(\mathbf{r}, t) = \sum_i B_i(\mathbf{r}, t),$$

$$\mathbf{u} = \frac{\sum_i f_i(\mathbf{r}, t)\mathbf{c}_i}{\rho} + \frac{\mathbf{F}}{2\rho},$$

where $\mathbf{F}$ is the surface tension inducing force, to be defined shortly. The color-blind density $\rho(\mathbf{r}, t) = \rho_R(\mathbf{r}, t) + \rho_R(\mathbf{r}, t)$ and $\tau \in [0.5, 2.0]$ is the collision parameter. Above, ρ, ρ_R, ρ_B, i, δ_t, $c_{i\alpha}$, t_i, u, and c_s denote overall nodal density, red fluid nodal density, blue fluid nodal density, link-index, time step, the α component of the ith lattice basis vector, the weight for link i, fluid velocity, and the color-blind speed of sound. The latter is a lattice property which, in LBGK models without density contrast, is a geometrical lattice tensor isotropy constant [see Eq. (16)].

We return to the matter of the mass activation parameter ϕ_i which must clearly be related to the speed of sound in the red and blue separated, ideal-gas components:

$$\phi_i = \begin{cases} \frac{\alpha_R\rho_R}{\rho} + \frac{\alpha_B\rho_B}{\rho}, & i = 0 \\ (1 - \alpha_R)\frac{s_i\rho_R}{\rho} + (1 - \alpha_B)\frac{s_i\rho_B}{\rho}, & i \neq 0. \end{cases} \tag{5}$$

In Eq. (5), s_i is a second link weight discussed in Sec. III and free parameters α_R and α_B are chosen to control the algorithm stability as well as the contrast in density between the red and

blue fluids:

$$\Lambda \equiv \frac{\rho_{0R}}{\rho_{0B}} = \frac{c_{sB}^2}{c_{sR}^2} = \frac{1-\alpha_B}{1-\alpha_R}. \tag{6}$$

Here, ρ_{0C} is the density deep within the color component $C \in [R, B]$ and the third part of the above equality (6) follows from the mechanical stability of the equilibrium red to blue ideal-gas interface, which requires $\rho_{0R}c_{sR}^2 = \rho_{0B}c_{sB}^2$. The physical speed of sound in the red (blue) phase is therefore identified as $c_{sR} = \kappa\sqrt{1-\alpha_R}$ ($c_{sB} = \kappa\sqrt{1-\alpha_B}$) with κ being a constant to be determined shortly. Now, it is important to note that $\lambda_R \to \lambda_B$ implies $\Lambda \to 1$; however, considering Eqs. (5) and (3), it is apparent that the traditional LBGK equilibrium [22] is recovered for $\alpha_R = \alpha_B = \frac{4}{9}$. In this model, the physical speed of sound, in lattice units, is $\frac{1}{3}$ (for D2Q9), so $\frac{1}{3} = \kappa^2(1-\frac{4}{9})$, which gives $\kappa = \sqrt{\frac{3}{5}}$ and hence

$$c_{sC} = \sqrt{\frac{3(1-\alpha_C)}{5}}, \quad C \in [R, B]. \tag{7}$$

We have chosen here to write the evolution in Eq. (2) in terms of the overall density but one can formulate this part of the algorithm in terms of colored densities individually [20].

The immiscible species in the simulation are identified by a generalized chromodynamic, or (sometimes) phase field, ρ^N [20] (to be further discussed),

$$\rho^N \equiv \frac{\left(\frac{\rho_R}{\rho_{0R}} - \frac{\rho_B}{\rho_{0B}}\right)}{\left(\frac{\rho_R}{\rho_{0R}} + \frac{\rho_B}{\rho_{0B}}\right)}, \tag{8}$$

in terms of which the macroscopic body force $\mathbf{F}$, is used to introduce interfacial tension effects, is be defined as

$$\mathbf{F} = \frac{1}{2}K\nabla\rho^N, \quad K = \nabla_s\rho^N, \tag{9}$$

where ∇_s denotes a numerical surface gradient [13].

Kinetic-scale, postcollision color species segregation, or color re-allocation, is an adaptation of the original method of d'Ortona *et al.* [14] which may be written as

$$C_i^{++}(\mathbf{r}, t) = \frac{\rho_C(\mathbf{r}, t)}{\rho(\mathbf{r}, t)} f_i(\mathbf{r}, t)^+ + \beta\frac{\phi_i(\mathbf{r}, t)\rho_R(\mathbf{r}, t)\rho_B(\mathbf{r}, t)}{\rho(\mathbf{r}, t)}\hat{\mathbf{n}}\cdot\delta_t\hat{\mathbf{c}}_i, \tag{10}$$

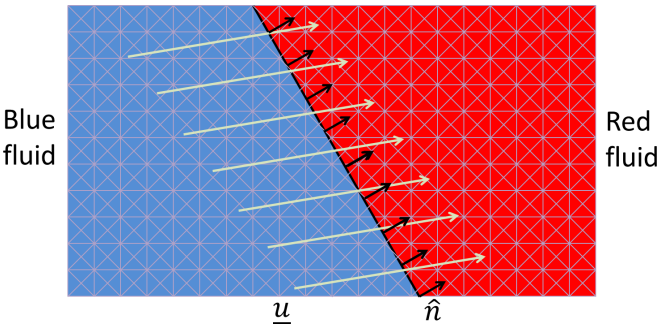

FIG. 1. A schematic representation of a flat interface between a pair of two-dimensional fluids designated red and blue. The red phase has larger density. $\hat{\mathbf{n}}$ is the interfacial normal, $\mathbf{u}$ is the uniform fluid motion, and the solid black interfacial line indicates the $\rho^N = 0$ contour. Note $\hat{\mathbf{n}}$ and $\mathbf{u}$ are not parallel.

where $C \in [R, B]$, superscript $+$ ($++$) denotes a post-collision (post-recolor) quantity and β is a chosen segregation parameter [14]. We note that this segregation rule is rigorously mass-conserving, simple to implement (it is algebraic), local (given a director, $\hat{\mathbf{n}}$), and, perhaps most significant, is "bottom-up," i.e., a kinetic scale postulate, which remains to be justified *a posteriori*.

III. MODEL KINEMATICS

Commencing from Eq. (10), we derive the continuum-scale kinematics for the scheme outlined in Sec. II. A circular interdependence between kinematics and dynamics is revealed as we proceed. Consider the two- or three-dimensional diphasic system represented schematically in Fig. 1. The interface is assumed flat and embedded within a uniformly moving fluid. Apply color conservation to a node at position $\mathbf{r}$, in order to relate red density at position $\mathbf{r}$, time $t + \delta_t$, to postcollision, post-recolor red link populations on adjacent nodes at the previous time step t:

$$\rho_R(\mathbf{r}, t+\delta_t) = \sum_{\forall i} R_i^{++}(\mathbf{r} - \delta_t\mathbf{c}_i, t). \tag{11}$$

Noting that, for a uniformly translating fluid in the interfacial region $f_i = f_i^{(0)}(\rho, \mathbf{u}) + F_{1i}$ (since, for an interface without curvature, $F_{2i} = 0$) we use the color re-allocation rule of Eq. (10):

$$\rho_R(\mathbf{r}, t+\delta_t) = \sum_{\forall i}\frac{\rho_R(\mathbf{r}-\delta_t\mathbf{c}_i)}{\rho(\mathbf{r}-\delta_t\mathbf{c}_i)}\left(f_i^{(0)}(\rho, \mathbf{u}) + F_{1i}\right) + \sum_{\forall i}\beta\frac{\phi_i(\mathbf{r}-\delta_t\mathbf{c}_i)\rho_R(\mathbf{r}-\delta_t\mathbf{c}_i)\rho_B(\mathbf{r}-\delta_t\mathbf{c}_i)\hat{\mathbf{n}}\cdot\delta_t\mathbf{c}_i}{\rho(\mathbf{r}-\delta_t\mathbf{c}_i)}. \tag{12}$$

Substituting for $f_i^{(0)}(\rho, \mathbf{u})$ from Eq. (3) to obtain

$$\rho_R(\mathbf{r}, t+\delta_t) = \sum_{\forall i}\left[\rho_R\phi_i + \frac{\rho_R}{\rho}F_{1i}\right]_{\mathbf{r}-\delta_t\mathbf{c}_i} + \sum_{\forall i}\left[t_i\rho_R\left(\frac{u_\alpha c_{i\alpha}}{c_s^2} + \frac{u_\alpha u_\beta c_{i\alpha}c_{i\beta}}{2c_s^4} - \frac{u^2}{2c_s^2}\right)\right]_{\mathbf{r}-\delta_t\mathbf{c}_i} + \delta_t\beta\sum_{\forall i}\left[\phi_i\left(\frac{\rho_R\rho_B}{\rho}\right)n_\beta c_{i\beta}\right]_{\mathbf{r}-\delta_t\mathbf{c}_i}. \tag{13}$$

Note that δ_t effectively labels spatial and temporal resolution here and that the term in F_{1i} originates from a source term in the dynamics, which, in the presence of a large density contrast, may be significant.

Now it is necessary to assume a form for the LDD correction term F_{1i}, to be derived in Sec. IV. Note that a need for tractability here motivates our use of LBGK dynamics. We choose the following projection onto the tensor Hermite

polynomials:

$$F_{1i} = t_i F_{\alpha\beta}\left(\rho_R,\ \rho_B,\ \rho^N,\ \Lambda, \mathbf{u}\right)\left(c_{i\alpha}c_{i\beta} - c_s^2\delta_{\alpha\beta}\right). \tag{14}$$

The advantages of this choice which will become apparent shortly. Replace ϕ_i in Eq. (13) by using the definitions in Eq. (5), Taylor expand all terms about $\mathbf{r}$, t to second order in δ_t, and, noting that there is no gradient in $\mathbf{u}$ by assumption, we collect terms, so that Eq. (13) becomes

$$\begin{aligned}
\rho_R + \delta_t\frac{\partial\rho_R}{\partial t} + \frac{1}{2}\delta_t^2\frac{\partial^2\rho_R}{\partial t^2} &= (1-\alpha_R)\sum_{i\neq 0} s_i\left[\frac{\rho_R^2}{\rho} - \delta_t c_{i\alpha}\partial_\alpha\left(\frac{\rho_R^2}{\rho}\right) + \frac{\delta_t^2}{2}c_{i\alpha}c_{i\beta}\partial_\alpha\partial_\beta\left(\frac{\rho_R^2}{\rho}\right)\right]\\
&+ (1-\alpha_B)\sum_{i\neq 0} s_i\left[\frac{\rho_R\rho_B}{\rho} - \delta_t c_{i\alpha}\partial_\alpha\left(\frac{\rho_R\rho_B}{\rho}\right) + \frac{\delta_t^2}{2}c_{i\alpha}c_{i\beta}\partial_\alpha\partial_\beta\left(\frac{\rho_R\rho_B}{\rho}\right)\right]\\
&+ \frac{\alpha_R\rho_R^2}{\rho} + \frac{\alpha_B\rho_B\rho_R}{\rho} + \frac{u_\gamma}{c_s^2}\sum_{\forall\, i} t_i\left[\rho_R - \delta_t c_{i\alpha}\partial_\alpha\rho_R + \frac{\delta_t^2}{2}c_{i\alpha}c_{i\beta}\partial_\alpha\partial_\beta\rho_R\right]c_{i\gamma}\\
&+ \frac{u_\alpha u_\beta}{2c_s^4}\sum_{\forall\, i} t_i\left[\rho_R - \delta_t c_{i\gamma}\partial_\gamma\rho_R + \frac{\delta_t^2}{2}c_{i\gamma}c_{i\delta}\partial_\gamma\partial_\delta\rho_R\right]c_{i\alpha}c_{i\beta}\\
&- \frac{u^2}{2c_s^2}\sum_{\forall\, i} t_i\left[\rho_R - \delta_t c_{i\alpha}\partial_\alpha\rho_R + \frac{\delta_t^2}{2}c_{i\alpha}c_{i\beta}\partial_\alpha\partial_\beta\rho_R\right]\\
&+ \sum_{\forall\, i} t_i\left[\frac{\rho_R F_{\alpha\beta}}{\rho} - \delta_t c_{i\gamma}\partial_\gamma\left(\frac{\rho_R F_{\alpha\beta}}{\rho}\right) + \frac{\delta_t^2}{2}c_{i\gamma}c_{i\delta}\partial_\gamma\partial_\delta\left(\frac{\rho_R F_{\alpha\beta}}{\rho}\right)\right]\left(c_{i\alpha}c_{i\beta} - c_s^2\delta_{\alpha\beta}\right)\\
&+ \delta_t\beta(1-\alpha_R)\sum_{i\neq 0} s_i\left[\frac{\rho_R^2\rho_B}{\rho^2} - \delta_t c_{i\alpha}\partial_\alpha\left(\frac{\rho_R^2\rho_B}{\rho^2}\right) + \frac{\delta_t^2}{2}c_{i\alpha}c_{i\beta}\partial_\alpha\partial_\beta\left(\frac{\rho_R^2\rho_B}{\rho^2}\right)\right]n_\gamma c_{i\gamma}\\
&+ \delta_t\beta(1-\alpha_B)\sum_{i\neq 0} s_i\left[\frac{\rho_R\rho_B^2}{\rho^2} - \delta_t c_{i\alpha}\partial_\alpha\left(\frac{\rho_R\rho_B^2}{\rho^2}\right) + \frac{\delta_t^2}{2}c_{i\alpha}c_{i\beta}\partial_\alpha\partial_\beta\left(\frac{\rho_R\rho_B^2}{\rho^2}\right)\right]n_\gamma c_{i\gamma}.
\end{aligned} \tag{15}$$

Note, in the above expression, the summations involving the t_i terms are on all values of link index i (e.g., $i = 0, 1, \ldots, 8$ in the case of D2Q9); however, those involving the s_i exclude the rest link, $i = 0$. The usual lattice isotropy properties are assumed:

$$\begin{aligned}
&\sum_{\forall\, i} t_i (c_{i\alpha})^{2p+1} = 0, \quad \sum_{\forall\, i} t_i c_{i\alpha}c_{i\beta} = c_s^2\delta_{\alpha\beta},\\
&\sum_{\forall\, i} t_i c_{i\alpha}c_{i\beta}c_{i\gamma}c_{i\theta} = c_s^4\Delta_{\alpha\beta\gamma\theta},
\end{aligned} \tag{16}$$

where p is any non-negative integer, $\delta_{\alpha\beta}$ is the Kronecker delta, and $\Delta_{\alpha\beta\gamma\theta} = \delta_{\alpha\beta}\delta_{\gamma\theta} + \delta_{\alpha\gamma}\delta_{\beta\theta} + \delta_{\alpha\theta}\delta_{\beta\gamma}$. For example, in the case of D2Q9, $t_{\text{rest}} = \frac{4}{9}$, $t_{\text{short}} = \frac{1}{9}$, $t_{\text{long}} = \frac{1}{36}$, and $c_s^2 = \frac{1}{3}$. Following Ba *et al.* we set

$$s_i = k t_i \quad (i \neq 0). \tag{17}$$

We can reserve similar properties for lattice tensors, weighted by s_i:

$$\sum_{i\neq 0} s_i (c_{i\alpha})^{(2p+1)} = 0, \tag{18}$$

$$\sum_{i\neq 0} s_i c_{i\alpha}c_{i\beta} = k c_s^2\delta_{\alpha\beta}, \tag{19}$$

$$\sum_{i\neq 0} s_i c_{i\alpha}c_{i\beta}c_{i\gamma}c_{i\theta} = k c_s^4\Delta_{\alpha\beta\gamma\theta}, \tag{20}$$

and we also follow Ba *et al.* and constrain the s_i in general as follows:

$$\sum_{i\neq 0} s_i = 1. \tag{21}$$

Now, note that the assumptions made in Eqs. (17) and (21) fix the value of k. For example, in D2Q9,

$$k = \frac{9}{5}, \tag{22}$$

and therefore k is not a parameter which may be tuned.

Using these assumptions, the resulting lattice properties given in Eqs. (18)–(20), Eq. (15) can be simplified to

$$\begin{aligned}
&\delta_t\frac{\partial\rho_R}{\partial t} + \frac{1}{2}\delta_t^2\frac{\partial^2\rho_R}{\partial t^2} + \delta_t u_\gamma\partial_\gamma\rho_R\\
&\quad= \frac{k}{2}c_s^2(1-\alpha_R)\delta_t^2\nabla^2\left(\frac{\rho_R^2}{\rho}\right) + \frac{k}{2}c_s^2(1-\alpha_B)\delta_t^2\nabla^2\left(\frac{\rho_R\rho_B}{\rho}\right)\\
&\qquad+ \frac{1}{2}\delta_t^2 u_\alpha u_\beta\partial_\alpha\partial_\beta\rho_R - \delta_t^2\beta(1-\alpha_R)kc_s^2 n_\gamma\partial_\gamma\left(\frac{\rho_R^2\rho_B}{\rho^2}\right)\\
&\qquad- \delta_t^2\beta(1-\alpha_B)kc_s^2 n_\gamma\partial_\gamma\left(\frac{\rho_R\rho_B^2}{\rho^2}\right)\\
&\qquad+ 2\delta_t^2 c_s^4\partial_\alpha\partial_\beta\left(\frac{\rho_R F_{\alpha\beta}}{\rho}\right),
\end{aligned} \tag{23}$$

in which the last term on the right-hand side originates in the density-difference correction term F_{1i}. Upon neglecting this term (see below), we have

$$\delta_t\frac{\partial\rho_R}{\partial t}+\frac{1}{2}\delta_t^2\frac{\partial^2\rho_R}{\partial t^2}+\delta_t u_\gamma\partial_\gamma\rho_R = \frac{k}{2}c_s^2(1-\alpha_R)\delta_t^2\nabla^2\left(\frac{\rho_R^2}{\rho}\right)+\frac{k}{2}c_s^2(1-\alpha_B)\delta_t^2\nabla^2\left(\frac{\rho_R\rho_B}{\rho}\right) + \frac{1}{2}\delta_t^2 u_\alpha u_\beta\partial_\alpha\partial_\beta\rho_R - \delta_t^2\beta(1-\alpha_R)kc_s^2n_\gamma\partial_\gamma\left(\frac{\rho_R^2\rho_B}{\rho^2}\right) - \delta_t^2\beta(1-\alpha_B)kc_s^2n_\gamma\partial_\gamma\left(\frac{\rho_R\rho_B^2}{\rho^2}\right). \quad (24)$$

Equation (24) may be supplemented by a second, independent equation formed by considering the blue species, which corresponds to applying the exchange symmetry $R\leftrightarrow B$, $\beta\rightarrow(-\beta)$ in Eq. (24). This and Eq. (24) furnish two equations in two unknown quantities, the macroscopic densities ρ_R and ρ_B.

We note that, for very small δ_t (which projects the most rapid color dynamics), Eq. (24) shows that ρ_R satisfies the first-order wave equation. Expressing this observation in terms appropriate for the Chapman-Enskog methodology to be used in Sec. IV, we have

$$\frac{\partial\rho_R}{\partial t_1}+u_\gamma\partial_\gamma\rho_R=0,\quad \frac{\partial\rho_B}{\partial t_1}+u_\gamma\partial_\gamma\rho_B=0, \quad (25)$$

with solution $\rho_C(\mathbf{x},t)=f(\mathbf{x}-\mathbf{u}t)$, $C\in[R,B]$. The directing or ordering influence of the interface (i.e., parameter $\hat{\mathbf{n}}$) appears on longer scales. However, at the very shortest scales, color apparently advects with the fluid. Put another way, color is a material invariant on the shortest timescales. This property of the model significantly influences the derivation of its dynamics, to which we now proceed.

IV. MODEL DYNAMICS

We require the simplicity of a LBGK scheme to exhibit the connection between model kinematics and dynamics. To this end, we avoid other complications, specifically, adjusting the equilibrium $f_i^{(0)}(\rho,\mathbf{u})$, i.e., we incorporate all LDD dynamics corrections in the evolution equation source term F_{1i}. Using assumptions based on the results in the previous section, then, we derive, by Chapman-Enskog expansion, a single-relaxation-time LBGK collision scheme for LDD MCLB.

A. Lattice Boltzmann Bhatnagar-Gross-Krook scheme for large density difference

It is convenient to use the transparent methodology of Guo *et al.* [16] and Hou *et al.* [23]. In the interest of a coherent literature, the overall structure of the analysis and notation is that of Guo *et al.* [16] and Hou *et al.* [23]. For definiteness we work in D2Q9, with $k=\frac{9}{5}$ and

$$s_i=kt_i\rightarrow\frac{9}{5}t_i. \quad (26)$$

We indicate modifications for three spatial dimensions below.

We assume the following moments of our equilibrium, after Ba *et al.*:

$$\sum_{i=0}^{Q}f_i^{(0)}(1,\ c_{i\alpha},\ c_{i\alpha}c_{i\beta})=(\rho,\ \rho u_\alpha,(2\phi_1+4\phi_2)\times\rho\delta_{\alpha\beta}+\rho u_\alpha u_\beta). \quad (27)$$

Functions ϕ_1 and ϕ_2 depend upon the chromodynamic field [see Eq. (5)] and hence the spatial-temporal variation of the isotropic term of the second moment is modified as $\sum_{i=0}^{Q}f_i^{(0)}c_{i\alpha}c_{i\beta}=\{\frac{3}{5}[(1-\alpha_R)\rho_R+(1-\alpha_B)\rho_B]\delta_{\alpha\beta}+\rho u_\alpha u_\beta\}$. Here, the variation of the speed of sound between red and blue components is apparent, with $c_{sR}^2=\frac{3}{5}(1-\alpha_R)$ and $c_{sB}^2=\frac{3}{5}(1-\alpha_B)$. The first order macroscopic equations (10 a) and (10 b) of Guo *et al.* [16] are recovered straightforwardly:

$$\frac{\partial\rho}{\partial t_1}+\partial_\alpha(\rho u_\alpha)=A_1=0,\qquad \frac{\partial\rho u_\alpha}{\partial t_1}+\partial_\alpha\Pi_{\alpha\beta}^{(0)}=\left(n+\frac{m}{\tau}\right)F_\alpha=F_\alpha, \quad (28)$$

provided $n+\frac{m}{\tau}=1$, $A_1=0$. Here, τ is the LBGK relaxation time. In the present context, the force $\mathbf{F}$ is the Navier-Stokes level immersed boundary force used to create interfacial tension effects. All other parameters have their usual meanings [16].

For LDD, the viscous flux $\Pi_{\alpha\beta}^{(1)}\equiv\sum_{i=0}^{Q}f_i^{(1)}c_{i\alpha}c_{i\beta}$ is transformed and Eq. (12) of Guo *et al.* may be written as

$$\left(\frac{\Pi_{\alpha\beta}^{(1)}}{\tau\delta_t}\right)=-(2\phi_1+4\phi_2)\frac{\partial\rho}{\partial t_1}\delta_{\alpha\beta}-\rho\frac{\partial}{\partial t_1}(2\phi_1+4\phi_2)\delta_{\alpha\beta} -\frac{\partial}{\partial t_1}\rho u_\alpha u_\beta -3\partial_\gamma\rho u_\delta\sum_{i=0}^{Q}t_ic_{i\alpha}c_{i\beta}c_{i\gamma}c_{i\delta} +\tfrac{1}{2}(C_{\alpha\beta}+C_{\beta\alpha}). \quad (29)$$

Here, the tensor $C_{\alpha\beta}$ is the correction introduced by Guo *et al.* [16], which is assigned so as to correct the dynamics. Previously, this correction did not account for the presence of large density gradients associated with the transition across the interface from a less to a more dense fluid. Therefore, for the present case of a density difference at the interface, we must carefully redefine this quantity $C_{\alpha\beta}$.

The usual procedure, now, is to replace time derivatives in Eq. (29) by invoking appropriate macroscopic dynamics. In the case of non-LDD LBGK, one utilizes the macroscopic dynamical Eq. (28). Here, transforming the isotropic terms in Eq. (29) requires determinate kinematics, as derived in Sec. III and expressed in Eq. (25). Using the value of $k=\frac{9}{5}$ for the D2Q9 lattice, Eq. (25) and the definition of ρ^N [Eq. (8)] it follows, after some straightforward but lengthy algebra,

$$\rho\frac{\partial}{\partial t_1}(2\phi_1+4\phi_2)=-\frac{6\rho}{5}q(\alpha_R-\alpha_B)\frac{\partial\rho^N}{\partial t_1}, \quad (30)$$

where we have defined

$$q\equiv\frac{\Lambda}{[(\Lambda-1)\rho^N+\Lambda+1]^2}. \quad (31)$$

It is now necessary further to refer to the kinematic properties of the model, previously for which we have already shown in Sec. III that color is a material invariant on the shortest timescales, i.e., $\frac{D}{Dt_1}\rho_R = \frac{D}{Dt_1}\rho_B = 0$, hence $\frac{D}{Dt_1}(\frac{\rho_R}{\rho_{0R}} \pm \frac{\rho_B}{\rho_{0B}}) = 0$ and consequently $\frac{D}{Dt}(\frac{\rho_R/\rho_{R0}-\rho_B/\rho_{B0}}{\rho_R/\rho_{R0}+\rho_B/\rho_{B0}}) = 0$ and so it follows from an application of the quotient rule that

$$\frac{D}{Dt_1}\rho^N = 0 \iff \frac{\partial \rho^N}{\partial t_1} = -u_\alpha \partial_\alpha \rho^N, \tag{32}$$

whereupon the time derivative may be eliminated from Eq. (30), yielding

$$\rho \frac{\partial}{\partial t_1}(2\phi_1 + 4\phi_2)\delta_{\alpha\beta} = \frac{6}{5}\rho q(\alpha_R - \alpha_B)\mathbf{u}\cdot\nabla\rho^N\delta_{\alpha\beta}, \tag{33}$$

and our expression for $\Pi^{(1)}_{\alpha\beta}$, Eq. (29), becomes

$$\begin{aligned}\left(\frac{\Pi^{(1)}_{\alpha\beta}}{\tau\delta_t}\right) = &-\frac{\rho}{3}(\partial_\alpha u_\beta + \partial_\beta u_\alpha)\\ &+ \Phi\partial_\gamma\rho u_\gamma\delta_{\alpha\beta} + u_\beta\partial_\alpha(\Phi\rho) + u_\alpha\partial_\beta(\Phi\rho)\\ &- u_\alpha F_\beta - u_\beta F_\alpha + \frac{1}{2}(C_{\alpha\beta} + C_{\beta\alpha})\\ &- \frac{6\rho}{5}q(\alpha_R - \alpha_B)\mathbf{u}\cdot\nabla\rho^N\delta_{\alpha\beta},\end{aligned} \tag{34}$$

where we have used the isotropy properties of the lattice and defined

$$\Phi \equiv 2\phi_1 + 4\phi_2 - \frac{1}{3}. \tag{35}$$

Equation (34) replaces Eq. (12) of Guo *et al.* [16]. We remark on the correct treatment of pressure terms in the second-order dynamics. It is very important to note that the isotropic term in the pressure tensor, Eq. (28), has not, as usual, entered the above expression for $\Pi^{(1)}_{\alpha\beta}$ precisely to correct the viscous stress term. Instead, to obtain the correct viscous stress in the model's dynamics, it is necessary to introduce the constant term in the definition above [Eq. (35)], which perturbs the steady interface profile.

It is now possible to write down an expression for the viscous stress tensor $\sigma'_{\alpha\beta}$. From Eq. (14) of Guo *et al.* we have $\sigma'_{\alpha\beta} = -(1-\frac{1}{2\tau})\Pi^{(1)}_{\alpha\beta} - \frac{\delta_t}{4}(C_{\beta\alpha} + C_{\alpha\beta})$ and hence using Eq. (34) we obtain

$$\begin{aligned}\sigma'_{\alpha\beta} = &\frac{\rho}{3}\left(1-\frac{1}{2\tau}\right)(\partial_\alpha u_\beta + \partial_\beta u_\alpha)\tau\delta_t\\ &-\left(1-\frac{1}{2\tau}\right)[\Phi\partial_\gamma\rho u_\gamma\delta_{\alpha\beta} + u_\beta\partial_\alpha(\Phi\rho)\\ &+ u_\alpha\partial_\beta(\Phi\rho)]\tau\delta_t\\ &+\left(1-\frac{1}{2\tau}\right)(u_\alpha F_\beta + u_\beta F_\alpha)\tau\delta_t\\ &-\left(1-\frac{1}{2\tau}\right)\frac{1}{2}(C_{\alpha\beta} + C_{\beta\alpha})\tau\delta_t\\ &-\frac{\delta_t}{4}(C_{\alpha\beta} + C_{\beta\alpha})\\ &+\left(1-\frac{1}{2\tau}\right)\frac{6}{5}\rho q(\alpha^R - \alpha^B)(\mathbf{u}\cdot\nabla\rho^N\delta_{\alpha\beta})\tau\delta_t.\end{aligned} \tag{36}$$

In Eq. (36) only the first term on the right-hand side is consistent with the Navier-Stokes equations. It is therefore possible to infer an error as follows:

$$\begin{aligned}E_{\alpha\beta} = &-\left(\tau-\frac{1}{2}\right)\delta_t[\Phi\partial_\gamma\rho u_\gamma\delta_{\alpha\beta} + u_\beta\partial_\alpha(\Phi\rho) + u_\alpha\partial_\beta(\Phi\rho)]\\ &+\left(\tau-\frac{1}{2}\right)\delta_t(u_\alpha F_\beta + u_\beta F_\alpha)\\ &-\frac{\tau}{2}\delta_t(C_{\alpha\beta} + C_{\beta\alpha})\\ &+\left(\tau-\frac{1}{2}\right)\delta_t\frac{6}{5}\rho q(\alpha^R - \alpha^B)\mathbf{u}\cdot\nabla\rho^N\delta_{\alpha\beta}.\end{aligned} \tag{37}$$

The following choice of tensor $C_{\alpha\beta}$ eliminates error $E_{\alpha\beta}$:

$$\begin{aligned}C_{\alpha\beta} = \left(1-\frac{1}{2\tau}\right)\Big[&u_\alpha[F_\beta - \partial_\beta(\Phi\rho)] + u_\beta[F_\alpha - \partial_\alpha(\Phi\rho)]\\ &- \Phi\partial_\gamma\rho u_\gamma\delta_{\alpha\beta} + \frac{6}{5}\rho q\Delta\alpha u_\gamma\partial_\gamma\rho^N\delta_{\alpha\beta}\Big],\end{aligned} \tag{38}$$

where, of course, $\Delta\alpha = (\alpha_R - \alpha_B)$. We note that, by setting $\alpha_R = \alpha_B$, $\Lambda \to 1$, $\partial_\beta\rho \to 0$, Eq. (38) above reduces to Eq. (16) of Guo *et al.*

Finally, now consider Eqs. (6) and (20) of Guo *et al.* for the evolution equation source term. We have found that, in the additional presence of large density gradients (which now characterize the interfacial region), the LBGK source term becomes

$$\begin{aligned}F_i \equiv t_i\Bigg\{&\left(1-\frac{1}{2\tau}\right)\frac{F_\alpha c_{i\alpha}}{c_s^2}\\ &-\frac{1}{2}\left(1-\frac{1}{2\tau}\right)\frac{1}{c_s^4}\Big[\Phi(\partial_\gamma\rho u_\gamma)\delta_{\alpha\beta}\\ &-\frac{6}{5}\rho q\Delta\alpha\partial_\gamma\rho^N u_\gamma\delta_{\alpha\beta} + u_\beta[\partial_\alpha(\Phi\rho) - F_\alpha]\\ &+ u_\alpha[\partial_\beta(\Phi\rho) - F_\beta]\Big]\left(c_{i\alpha}c_{i\beta} - c_s^2\delta_{\alpha\beta}\right)\Bigg\},\end{aligned} \tag{39}$$

that is, in separated form, first for the density-difference correction:

$$\begin{aligned}F_{1i} = &-\frac{1}{2}t_i\left(1-\frac{1}{2\tau}\right)\frac{1}{c_s^4}\\ &\times\Big[\Phi\partial_\gamma(\rho u_\gamma)\delta_{\alpha\beta} - \frac{6}{5}\rho q\Delta\alpha\partial_\gamma(\rho^N u_\gamma)\delta_{\alpha\beta} + u_\beta\partial_\alpha(\Phi\rho)\\ &+ u_\alpha\partial_\beta(\Phi\rho)\Big]\left(c_{i\alpha}c_{i\beta} - c_s^2\delta_{\alpha\beta}\right),\end{aligned} \tag{40}$$

and, second, for the immersed boundary force

$$\begin{aligned}F_{2i} = &\,t_i\left(1-\frac{1}{2\tau}\right)\\ &\times\left[\frac{F_\alpha c_{i\alpha}}{c_s^2} + \frac{(u_\beta F_\alpha + u_\alpha F_\beta)\left(c_{i\alpha}c_{i\beta} - c_s^2\delta_{\alpha\beta}\right)}{c_s^4}\right].\end{aligned}$$

The preceding Chapman-Enskog treatment of the correction of the emergent dynamics is based upon a relatively simple single-relaxation-time LBGK model after Qian *et al.*

[22] and Guo *et al.* [16]. Ba *et al.* derived an equivalent scheme based upon a multiple-relaxation-time LB variant, after Lallemand and Luo [24]. One could also derive schemes based upon inverse multiple-relaxation-time LB variants [25,26]. However, all would contain equivalent evolution equation source terms, i.e., those independent of F_β in Eq. (39).

B. Extension to three spatial dimensions

Our analysis above generalizes straightforwardly to other LBGK collision schemes on lattices of different dimensionality. For example, in the case of D3Q19, the following simple replacements in Eq. (40) are easily determined:

$$k \to \frac{3}{2}, \quad (2\phi_1 + 4\phi_2) \to (2\phi_1 + 8\phi_2). \tag{41}$$

V. RESULTS

In the two previous sections, we derived interdependent dynamics and kinematics for a LDD chromodynamic MCLB model—a process streamlined by our use of LBGK dynamics. Henceforward, we focus on model kinematics, noting that our discussions should be seen in the supporting context of the work of Ba *et al.* and Liu *et al.*, who successfully demonstrated the utility of the segregation scheme analyzed here by using more robust MRT variants, [20,21]. Specifically, we seek to assess model kinematics and understand its reliance on underlying dynamics and by considering other, more sophisticated MRT collision schemes. Clearly, it is appropriate to begin by seeking solutions to Eq. (24), the form of which is of central importance because the stability of the method rests upon numerical derivatives of the profile shape and hence its differentiability, i.e., smoothness.

A. Steady solution

We seek steady solutions to Eq. (24) by considering a steady interface, separating two fluids at rest. An exact solution is possible. We consider only lattices which conform with the properties expressed in Eqs. (17)–(21). Let $\mathbf{u} = 0$ and $\frac{\partial \rho_R}{\partial t} = \frac{\partial^2 \rho_R}{\partial t^2} = 0$. In this "steady" three-dimensional case, Eq. (23) reduces to the following partial differential equation:

$$0 = kc_s^2\left[\frac{1}{2}\nabla^2\left(\frac{\rho_R^2}{\rho}\right) + \frac{1}{2}\left(\frac{1-\alpha_B}{1-\alpha_R}\right)\nabla^2\left(\frac{\rho_R\rho_B}{\rho}\right) - \beta n_\gamma \partial_\gamma\left(\frac{\rho_R^2\rho_B}{\rho^2}\right) - \beta\left(\frac{1-\alpha_B}{1-\alpha_R}\right)n_\gamma\partial_\gamma\left(\frac{\rho_R\rho_B^2}{\rho^2}\right)\right]. \tag{42}$$

In Appendix A we further reduce to one dimension (1D) and show by direct integration of the resulting ordinary differential equation that the one-dimensional steady solution is $\rho_R = \frac{\rho_{0R}}{2}[1 + \tanh(\beta x)]$ and $\rho_B = \frac{\rho_{0B}}{2}[1 - \tanh(\beta x)]$, which one can generalize to three dimensions, to obtain a trial solution of Eq. (42):

$$\rho_R = \frac{\rho_{0R}}{2}[1 + \tanh(\beta\hat{\mathbf{n}}\cdot\mathbf{x})], \quad \rho_B = \frac{\rho_{0B}}{2}[1 - \tanh(\beta\hat{\mathbf{n}}\cdot\mathbf{x})]. \tag{43}$$

The above solution may be verified by differentiation and substitution. The lengthy algebra is facilitated by eliminating differentiation, using properties of Eq. (43) such as $\partial_\alpha\rho_R = \frac{\rho_{0R}\beta\hat{\mathbf{n}}_\alpha}{2}\mathrm{sech}^2(\beta\hat{\mathbf{n}}\cdot\mathbf{x}) = \frac{2\rho_{0R}\beta\hat{\mathbf{n}}_\alpha}{\rho_{0B}}\rho_R\rho_B$. Note that this solution is exact, isotropic (valid for any orientation $\hat{\mathbf{n}}$), and valid for any value Λ of density contrast.

B. Unsteady solutions

Let us consider the case of the kinematic conditions obeyed by an interface separating two immiscible, uniformly translating components. We will consider the exact solution to a small density contrast approximation, followed by the general solution. In general, an exact solution to Eq. (24) cannot be found.

1. Approximate solution

We proceed to an approximate solution of the interface motion by excluding the terms in Eq. (24) which contain (derivatives of) the dynamics correction terms $F_{\alpha\beta}$. This simplification led to the following, recall:

$$\begin{aligned}\delta_t\frac{\partial\rho_R}{\partial t} + \frac{1}{2}\delta_t^2\frac{\partial^2\rho_R}{\partial t^2} + \delta_t u_\gamma\partial_\gamma\rho_R &= \frac{k}{2}c_s^2(1-\alpha_R)\delta_t^2\nabla^2\left(\frac{\rho_R^2}{\rho}\right) + \frac{k}{2}c_s^2(1-\alpha_B)\delta_t^2\nabla^2\left(\frac{\rho_R\rho_B}{\rho}\right) \\ &+ \frac{1}{2}\delta_t^2 u_\alpha u_\beta\partial_\alpha\partial_\beta\rho_R \\ &- \delta_t^2\beta(1-\alpha_R)kc_s^2 n_\gamma\partial_\gamma\left(\frac{\rho_R^2\rho_B}{\rho^2}\right) \\ &- \delta_t^2\beta(1-\alpha_B)kc_s^2 n_\gamma\partial_\gamma\left(\frac{\rho_R\rho_B^2}{\rho^2}\right),\end{aligned} \tag{44}$$

which is justified *a priori* by observing that these terms arise from the source term F_{1i} in Eq. (2), which for stability must be relatively small. We revisit this assumption below.

The solution to the approximate unsteady, three-dimensional problem of Eq. (44) is readily obtained from an obvious generalization of Eq. (43):

$$\begin{aligned}\rho_R &= \frac{\rho_{0R}}{2}\{1 + \tanh[\beta\hat{\mathbf{n}}\cdot(\mathbf{x} - \mathbf{u}t)]\}, \\ \rho_B &= \frac{\rho_{0B}}{2}\{1 - \tanh[\beta\hat{\mathbf{n}}\cdot(\mathbf{x} - \mathbf{u}t)]\}, \\ \rho &= \rho_R + \rho_B,\end{aligned} \tag{45}$$

which, after lengthy algebra, may be verified by differentiation and substitution into Eq. (23). Significantly, a chromodynamic field defined following Eq. (21) of Ba *et al.*,

$$\rho^N \equiv \frac{\left(\frac{\rho_R}{\rho_{0R}} - \frac{\rho_B}{\rho_{0B}}\right)}{\left(\frac{\rho_R}{\rho_{0R}} + \frac{\rho_B}{\rho_{0B}}\right)} \to \tanh[\beta\hat{\mathbf{n}}\cdot(\mathbf{x} - \mathbf{u}t)], \tag{46}$$

may now be seen to possess physically correct behavior in the presence of a density difference (as long as our approximations remain valid) whereas the usual definition, $\rho^N = \frac{\rho_R - \rho_B}{\rho_R + \rho_B}$, will not. Note that there is a conserved quantity:

$$\frac{\rho_R}{\rho_{0R}} + \frac{\rho_B}{\rho_{0B}} = 1 \iff \rho_R + \Lambda\rho_B = \rho_{0R}. \tag{47}$$

Henceforth, we shall refer to the approximate solution in Eq. (45), obtained in this section, as the equilibrium interface solution.

2. Advection error

Let us estimate the size and properties of previously neglected error term in Eq. (23) by substituting from Eq. (40) and the equilibrium interface solution in Eq. (45). After lengthy but straightforward algebra, we obtain

$$\begin{aligned}\Delta &= \left[2\delta_t^2 c_s^4 \partial_\alpha \partial_\beta \left(\frac{\rho_R F_{\alpha\beta}}{\rho}\right)\right]_{\rm eq} \\ &= -2\delta_t^2\left(1-\frac{1}{2\tau}\right) \\ &\quad\times\left[\partial_\alpha\partial_\beta\frac{\rho_R}{\rho}\left(u_\alpha\partial_\beta\rho+u_\beta\partial_\alpha\rho+u_\gamma\partial_\gamma\rho\delta_{\alpha\beta}\right)\right]_{\rm eq} \\ &= -4\beta\delta_t^2\left(1-\frac{1}{2\tau}\right)\left(\frac{1}{\rho_{0B}}-\frac{1}{\rho_{0R}}\right) \\ &\quad\times\left[(\hat{\mathbf{n}}\cdot\boldsymbol{\nabla})(\mathbf{u}\cdot\boldsymbol{\nabla})+\hat{\mathbf{n}}\cdot\mathbf{u}\nabla^2\right)\left[\frac{\rho_R^2\rho_B}{\rho}\right]_{\rm eq},\end{aligned} \tag{48}$$

which vanishes for $\hat{\mathbf{n}}\cdot\mathbf{u}=0$ (because in this geometry stream-wise variation is tangent to the interface). Hence, the approximate "equilibrium" solution remains exact in this geometry and the above advection error vanishes when flow is tangent to the interface, as well as in the limit of no density contrast, $\rho_{0B}=\rho_{0R}$. We return to this matter in Sec. V C 2.

Let us bound the size of the advection equation error, defined above. Derivative $\partial_\beta\rho$ will clearly take its largest value mid-interface, hence $\max(\partial_\beta\rho)\approx\frac{(\Lambda\rho_{0B}-\rho_{0B})}{1/\beta}=\beta(\Lambda-1)\rho_{0B}$, also $\max(\rho_R/\rho)=1$, so omitting factors of order unity we estimate, for $\Lambda>10$, from the first of Eq. (48),

$$\Delta<\left(1-\frac{1}{2\tau}\right)\beta u(\Lambda-1)\rho_{0B}. \tag{49}$$

3. Comparison with multi-relaxation time

Ba *et al.* devised the segregation for which we determine the chromodynamic field dynamics above—but based upon a MRT collision model. We now consider the kinematics of this MRT model which, owing to its increased sophistication, is much more difficult to treat than our LBGK model, which was developed to facilitate analysis. With the MRT collision scheme developed by Ba *et al.*, the equivalent of Eqs. (23) and (48) are significantly complicated [see Appendix B, Eq. (B9), where, using the steps documented above, we derived the continuum-scale MRT kinematics]. By neglecting the terms in the two relevant MRT relaxation parameters, s_v and s_e (which replace LBGK relaxation parameter τ), we obtain the previous solution and model kinematics. The neglected terms define a MRT scheme advection error:

$$\begin{aligned}\Delta &= \frac{k\delta_t^2}{12}(1-\alpha_R)\left(1-\frac{s_e}{2}\right)u_\alpha\partial_\alpha\nabla^2\left(\frac{\rho_R^2}{\rho}\right) \\ &\quad+\frac{k\delta_t^2}{12}(1-\alpha_B)\left(1-\frac{s_e}{2}\right)u_\alpha\partial_\alpha\nabla^2\left(\frac{\rho_R\rho_B}{\rho}\right) \\ &\quad-\frac{\delta_t^2}{12k}\left(1-\frac{s_e}{2}\right)u_\alpha\partial_\alpha\nabla^2\rho \\ &\quad+\frac{5k\delta_t^2}{36}(1-\alpha_R)\left(1-\frac{s_v}{2}\right)\epsilon_{z\alpha\beta}u_\alpha\partial_\beta\left(\partial_x^2-\partial_y^2\right)\left(\frac{\rho_R^2}{\rho}\right) \\ &\quad+\frac{5k\delta_t^2}{36}(1-\alpha_B)\left(1-\frac{s_v}{2}\right)\epsilon_{z\alpha\beta}u_\alpha\partial_\beta\left(\partial_x^2-\partial_y^2\right)\left(\frac{\rho_R\rho_B}{\rho}\right) \\ &\quad-\frac{\delta_t^2}{4k}\left(1-\frac{s_v}{2}\right)\epsilon_{z\alpha\beta}u_\alpha\partial_\beta\left(\partial_x^2-\partial_y^2\right)\rho.\end{aligned} \tag{50}$$

$$\begin{aligned}&-\frac{\delta_t^2}{12k}\left(1-\frac{s_e}{2}\right)u_\alpha\partial_\alpha\nabla^2\rho \\ &+\frac{5k\delta_t^2}{36}(1-\alpha_R)\left(1-\frac{s_v}{2}\right)\epsilon_{z\alpha\beta}u_\alpha\partial_\beta\left(\partial_x^2-\partial_y^2\right)\left(\frac{\rho_R^2}{\rho}\right) \\ &+\frac{5k\delta_t^2}{36}(1-\alpha_B)\left(1-\frac{s_v}{2}\right)\epsilon_{z\alpha\beta}u_\alpha\partial_\beta\left(\partial_x^2-\partial_y^2\right)\left(\frac{\rho_R\rho_B}{\rho}\right) \\ &-\frac{\delta_t^2}{4k}\left(1-\frac{s_v}{2}\right)\epsilon_{z\alpha\beta}u_\alpha\partial_\beta\left(\partial_x^2-\partial_y^2\right)\rho.\end{aligned} \tag{51}$$

We note that the velocity-dependent terms in the above do not reduce to the form $\hat{\mathbf{n}}\cdot\mathbf{u}$, close to equilibrium. Hence, advection error will not, for an MRT scheme, vanish for motion tangent to the interface.

We proceed to the bound, as Sec. V B 2, for the case of motion perpendicular to the interface $\mathbf{u}=u\hat{e}_x$, $\hat{\mathbf{n}}=\hat{e}_x$, taking $\delta_t=1$. The terms in $(1-\frac{s_e}{2})$ above transform to $\frac{k}{12}u\frac{d^3}{dx^3}(\frac{[(1-\alpha_R)\rho_R+(1-\alpha_B)\rho_B]\rho_R}{\rho})+\frac{1}{12k}u\frac{d^3}{dx^3}\rho$, and using the approximate result $[(1-\alpha_R)\rho_R+(1-\alpha_B)\rho_B]\approx\rho_{0R}$ (see next section) to $\frac{k}{12}u(1-\alpha_R)\rho_{R0}\frac{d^3}{dx^3}\frac{\rho_R}{\rho}+\frac{1}{12k}u\frac{d^3}{dx^3}\rho$. Following the estimates used in the last section, it is easily shown that both these terms may be approximated by the expression $(1-\frac{s_e}{2})u\beta\Lambda\rho_{B0}$. We estimate the terms in $(1-\frac{s_v}{2})$ similarly, as $(1-\frac{s_v}{2})u\beta\Lambda\rho_{B0}$. Accordingly, in place of Eq. (49) for the LBGK collision, we find for an MRT scheme:

$$\Delta<\max\left(\left(1-\frac{s_e}{2}\right),\left(1-\frac{s_v}{2}\right)\right)\beta u\Lambda\rho_{0B}, \tag{52}$$

which is, as might be expected, equivalent to that obtained with the LBGK scheme.

4. Stability

Clearly, the colored distribution functions, R_i and B_i must be positive on physical grounds. Let us investigate the requirement of $R_i>0$ constraint. From Eq. (10), with $\delta_t=1$, it is immediate that for $R_i^{++}>0$ we must have

$$\frac{\rho_R(\mathbf{r},t)}{\rho(\mathbf{r},t)}f_i^+(\mathbf{r},t)>\beta\frac{\phi_i(\mathbf{r},t)\rho_R(\mathbf{r},t)\rho_B(\mathbf{r},t)}{\rho(\mathbf{r},t)}\hat{\mathbf{n}}\cdot\underline{c}_i, \tag{53}$$

and substituting for a uniformly translating fluid $f_i^+(\mathbf{r},t)\approx\rho\phi_i+t_i\rho\frac{\mathbf{u}\cdot\underline{c}_i}{c_s^2}$, we find $(1+t_i\rho\frac{\mathbf{u}\cdot\underline{c}_i}{c_s^2})>\beta\frac{\rho_B(\mathbf{r},t)}{\rho(\mathbf{r},t)}\hat{\mathbf{n}}\cdot\underline{c}_i\delta_t$. Since $\frac{\rho_B(\mathbf{r},t)}{\rho(\mathbf{r},t)}<1$, $\max(\hat{\mathbf{n}}\cdot\underline{c}_i)=\cos(\pi/4)$ (for D2Q9) and, neglecting motion, we find the following stability condition on the component segregation parameter:

$$\beta<\frac{1}{\sqrt{2}}, \tag{54}$$

which is well supported over a range of simulation results. Hence, stability is seen to bound interface width. This observation accords with Eq. (49) for the advection error.

C. Numerical results

The emphasis here is on LDD kinematics but we include in this section some consideration of the dynamics of our LBGK scheme of Sec. 4. Predictions of advection error Δ in Eqs. (49) and (52) for LBGK and MRT, respectively, are very similar. Therefore, while all data presented in this

TABLE I. Maximum microcurrent velocity (in lattice units) for a static droplet of initial radius $R = 20$ in a domain of 80×80, for $\Lambda \in [10^{-3}, 10^{3}]$, $\beta = 0.67$ with curvature K fixed at $\frac{1}{R}$. Simulation corresponds to the LBGK collision model of Sec. IV.

Static drop microcurrent: curvature K fixed			
Λ	α_B	α_R	$10^5 \lvert\mathbf{u}\rvert_{\max}$
0.001	0.9995	0.5	9.414
0.01	0.995	0.5	1.076
0.1	0.95	0.5	4.955×10^{-4}
10	0.5	0.95	3.389×10^{-4}
100	0.5	0.995	1.709
1000	0.5	0.9995	6.620

section relate to our LBGK scheme, it should apply without significant modification to a MRT-based chromodynamic MCLB variant. Throughout, we avoid compressibility error by ensuring the simulations' Mach number, Ma, based on the dense component speed of sound (with the smallest value) is bounded as

$$\mathrm{Ma} = \frac{u}{\min\left(c_{sR}, c_{sB}\right)} < 0.06. \tag{55}$$

1. Microcurrent

The microcurrent is an unphysical flow induced by the surface-tension immersed boundary force in chromodynamic MCLB and by equivalent mechanisms in other MCLB variants.

Let us consider a static drop, initial radius R. (No confusion should arise with R_i, the red density associated with link i.) Let $\mathbf{u} = \mathbf{0}$: all flow is then due to the microcurrent. While Eq. (49) predicts that one can achieve large Λ when u is small, one must expect large density gradients in interface region to increase numerical errors associated with gradient calculations which generate effect. For chromodynamic MCLB with $\Lambda = 1$, microcurrent flow is greatly reduced when numerical computation of local curvature K is obviated by replacing $K \to \frac{1}{R}$ [see Eq. (9)] and also when β is reduced [27]. Tables I and II record the maximum microcurrent velocity (in lattice units) for a static droplet of radius $R = 20$ in a domain of 80×80, for $\Lambda \in [10^{-3}, 10^{3}]$, $\beta = 0.67$ with K fixed and measured, respectively. For these these data, the red fluid

TABLE II. Maximum microcurrent velocity (in lattice units) for a static droplet of initial radius $R = 20$ in a domain of 80×80, for $\Lambda \in [10^{-3}, 10^{3}]$, $\beta = 0.67$ with calculated curvature K. Simulation corresponds to the LBGK collision model of Sec. IV.

Static drop microcurrent: curvature K calculated			
Λ	α_B	α_R	$10^5 \lvert\mathbf{u}\rvert_{\max}$
0.001	0.9995	0.5	9.402
0.01	0.995	0.5	2.913
0.1	0.95	0.5	1.153×10^{-1}
10	0.5	0.95	1.824×10^{-2}
100	0.5	0.995	1.736
1000	0.5	0.9995	6.208

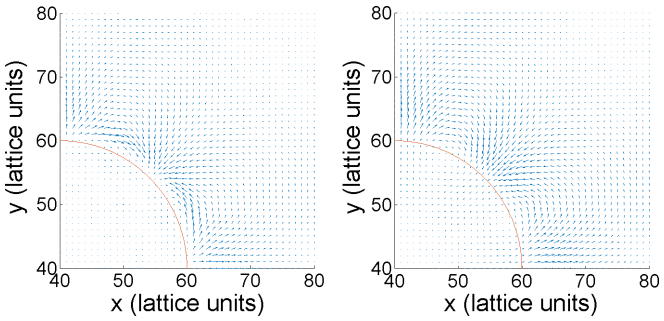

FIG. 2. Normalized microcurrent flow for $\Lambda = 10$ in the vicinity of a drop of radius $R = 20$ for (a) fixed $K = \frac{1}{R}$ and (b) numerically calculated curvature. See Tables I and II for the corresponding absolute velocities. The circulation in the case of fixed curvature is more localized.

comprises the droplet. For $\Lambda \in [10^{-1}, 10]$ we see the expected benefits of setting $K = \frac{1}{R}$ evaporate as, presumably, numerical error associated with the computation of increasingly large interfacial density gradients overwhelms other errors. These data compare well with that of Ba *et al.*, who report microcurrent activity using their MRT based model.

Figure 2 below compares the microcurrent flow at $\Lambda = 10$ for calculated and fixed curvatures. Flow field vectors are normalized in each plot. The flow in the case of fixed curvature is actually much weaker (refer to Tables I and II) and more restricted to the interfacial region.

2. Kinematics

The analysis in Sec. V B 2 explains the ability of the phase-field method to achieve very large density differences for small u. Inequality (49) implies that, to bound advection error, as the fluids' density contrast increases the velocity and width of the interface must decrease. For the data presented in this section we choose to consider a narrow interface characterized by $\beta = 0.68$ (which is representative of a practical, narrow interface) and we consider a flat interfaces, without interfacial tension with $\hat{\mathbf{n}} = \hat{e}_x$. From Eq. (45) we have for such a system

$$\rho_{0B} = \rho_B(x) + \frac{\rho_R(x)}{\Lambda}. \tag{56}$$

We test our model of the kinematics of chromodynamic MCLB by considering two cases-motion parallel and perpendicular to a flat interface. For the former case, $\hat{\mathbf{n}} \cdot \mathbf{u} = 0$ and Eq. (49) predicts zero advection error. Here, tests on a flat interface embedded in a uniformly translating fluid show negligible error for a very wide range of Λ and u. Consider the more interesting case of $\hat{\mathbf{n}} \cdot \mathbf{u} = u$ now. For the data presented in Figs. 3 and 4, for both fluids, $\tau = 1$, $\nu = \frac{1}{6}(2\tau - 1)$, $\beta = 0.65$, $\sigma = 0.01$ (though the interface is flat, note), $\alpha_B = 0.1$ and $\alpha_R \in [0.1, 0.9991]$ (giving $\Lambda \in [1, 1000]$). Other parameters are as discussed. In Fig. 3 we show simulation data and theory for the case of a static density contrast of $\Lambda = \rho_{0R} = 10$. For this system, the equilibrated flat interface was found centered upon $x = 19.53$. ρ_C, where $C \in [R, B]$, denotes the colored density, which is measured in lattice units. Figure 3(a) shows the red (denser fluid) and blue density profiles in the region of the interface, with the

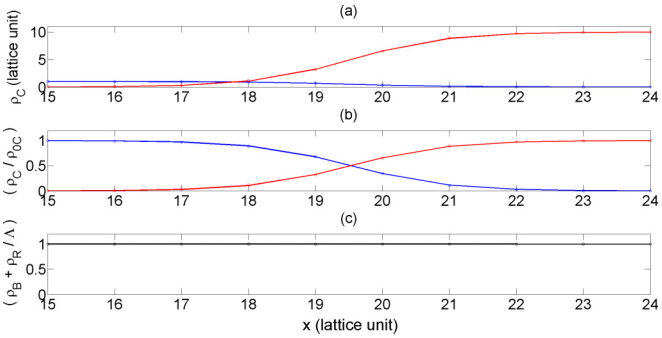

FIG. 3. Static interface data for a density contrast of $\Lambda = \rho_{0R} = 10$. Solid red (blue) line correspond to a model based on Eq. (45). Red (blue) open circles correspond to data for the red (blue) fluid. The equilibrated flat interface was centered upon $x = 19.53$. ρ_C denotes the colored density, which is measured in lattice units. (a) Red (denser fluid) and blue density profiles in the region of the interface. Continuous lines correspond to the variation predicted by Eq. (45). (b) Normalized density profiles. (c) A test of Eq. (56).

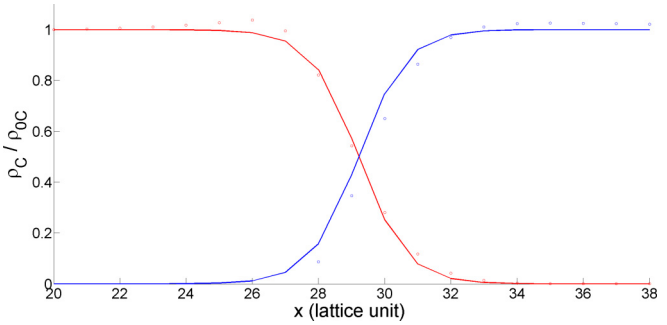

FIG. 5. Onset of numerical instability. See Fig. 3 caption for key. For these data, advection speed $u_0 = 0.15c_s$, $\Lambda = \rho_{0R} = 10$. The red fluid moves right, displacing the lighter fluid. Interfacial structure departs from that predicted significantly. Note, however, that this profile remains stable and advects at the correct speed. For this reason it is taken to define the case of marginal stability (see Fig. 6).

continuous lines corresponding to the variation predicted by Eq. (45). Figure 3(b) shows normalized density profiles $\frac{\rho_C}{\rho_{0C}}$ and Fig. 3(c) shows the result of a test of Eq. (56). Static interface profiles for density contrast parameters $\Lambda \leqslant 500$ also show good agreement with the predictions of Sec. III.

We consider next an advecting interface and seek to confirm that its profile advects without shape-transformation. Shape invariance for a range of Λ is addressed in Fig. 4. These data were obtained as follows: At $t = 0$, apply uniform flow u_0 to a previously equilibrated profile. Figure 4 shows instantaneous interface profiles at time $t = \frac{20}{u_0}$, i.e., at a time taken to move 20 nodes in the direction of the interfacial normal. A range of u_0 and Λ is considered. The value of u_0 is expressed as a multiple of model color-blind speed of sound, c_s. Recall that, for LB, the maximum value of flow velocity $u_{\max} < 0.15c_s$. For physically accurate behavior, consistent with the kinematic condition of mutual impenetrability, the interface should advect without dispersion, at the same speed as the fluid. Hence the colored density profile evolution should be described by

$$\frac{\rho_R(x)}{\Lambda} = \frac{1}{2}[1 + \tanh(x - u_0 t)],$$
$$\rho_B(x) = \frac{1}{2}[1 - \tanh(x - u_0 t)]. \tag{57}$$

Results in Fig. 4 show excellent agreement between simulation data and predicted profiles in Eq. (57) above. In these data the denser, red component is situated on the left and moves toward the right.

As one might expect, instability begins with profile distortion. As discussed above, this distortion arises in the interac-

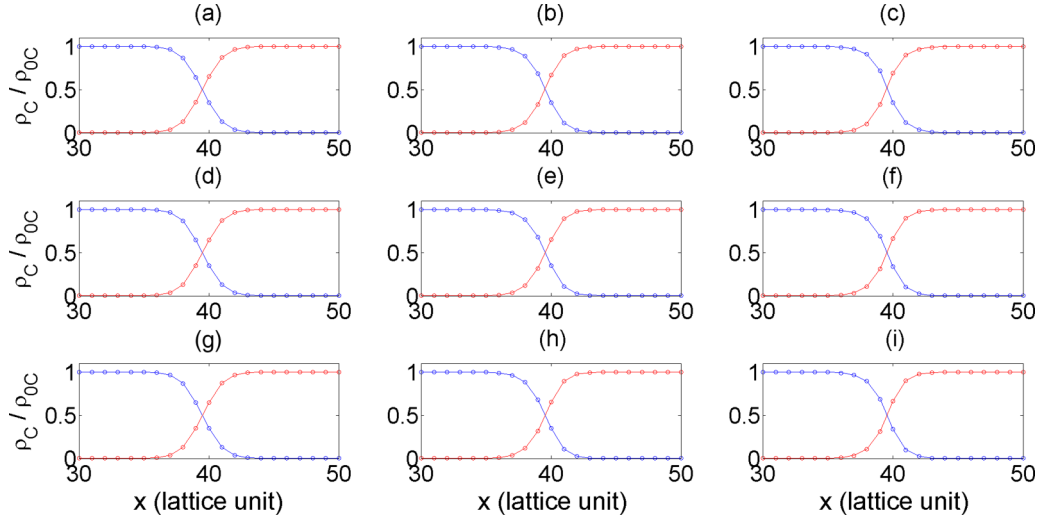

FIG. 4. Advection tests. See Fig. 3 caption for key. The initial, equilibrated, flat interface was centered close to $x = 20$. ρ_C denotes the colored density. The figure shows the result of applying flow $u_0\hat{e}_x$ and allowing the interface to advect 20 lattice units. Panels (a)–(c) correspond to $\Lambda \in [1, 10, 20]$, advection speed $u_0 = 1.5 \times 10^{-2}c_s$, panels (d)–(f) correspond to $\Lambda \in [1, 10, 20]$, advection speed $u_0 = 1.5 \times 10^{-3}c_s$, panels (g)–(i) correspond to $\Lambda \in [1, 10, 20]$, advection speed $u_0 = 1.5 \times 10^{-4}c_s$. It is clear that, for a range of u_0 and Λ, the interface structure conforms with that predicted.

$\frac{u_0}{c_s}$	Λ					
	1	10	25	50	100	1000
0.15	< 1.38	unstable	unstable	unstable	unstable	unstable
0.015	< 1.38	< 1.38	< 1.38	< 1.38	unstable	unstable
0.0015	< 1.38	< 1.38	< 1.38	< 1.38	< 1.38	< 1.38
0.00015	< 1.38	< 1.38	< 1.38	< 1.38	< 1.38	< 1.38

FIG. 6. Stability of scheme indicated by value of $\Delta(t)^2 \times 10^3$ in Eq. (58). Gray-shaded cells correspond to cases considered in Fig. 4. Stable cases had values of $\Delta(t)^2 \times 10^3 < 1.38$. Cases of large, unphysical profile distortion are indicated by orange shading. Note that very large density differences may be achieved at small advection speed. Refer to Fig. 5 with respect to the marginal case $\Lambda = 10, u_0 = 0.15c_s$.

tion of segregation and source term in the evolution equation. Apparently, instability is first manifested when a denser (red) component displaces a lighter (blue) component. Figure 5 shows what we designate a marginal profile which departs significantly from the predicted profile (but still advects at the correct speed, note). In these data, the denser, red component is situated on the left and moves towards the right. By adjusting parameters in accord with criterion (49), e.g., by reducing β, this effect may be removed. Note, however, that increasing β introduces an unphysical scale into simulations [28].

The advecting profile distortion is quantified as follows:

$$\Delta(t)^2 \equiv \sum_i \left\{ \rho_R(x_i, t) - \frac{\rho_{0R}}{2}[1 + \tanh(x_i - u_0 t)] \right\}^2, \quad (58)$$

where summation occurs over a range of 40 locations x_i which span the interface. The t origin was positioned to fit the equilibrated profile. All results in Fig. 4 have $\Delta(t)^2 < 1.38 \times 10^{-3}$ and are considered stable. The result in Fig. 5 has $\Delta(t)^2 = 0.976$. This profile still advects at speed u_0 but it departs recognizably from a tanh profile. We choose this profile's value of $\Delta(t)^2 = 0.976$ to represent a marginal case, since its shape is stable and its advection speed is correct but further increase in Λ rapidly leads to unphysical profile shape and instability (see Fig. 6).

Equation (49) suggests that the onset of instability arising from the kinematics of the model, in contradistinction to that due, e.g., to compressibility error, should occur for small Ma and with profile advection speed and density contrast in the approximate relationship $u \sim \frac{1}{\Lambda - 1}$. The data in Fig. 7 verify the predicted linear relationship between Λ and speed u at which a flat interface develops an error of 5%, according to Eq. (58) above. For these data, $\hat{\mathbf{n}} \cdot \mathbf{u} = u$.

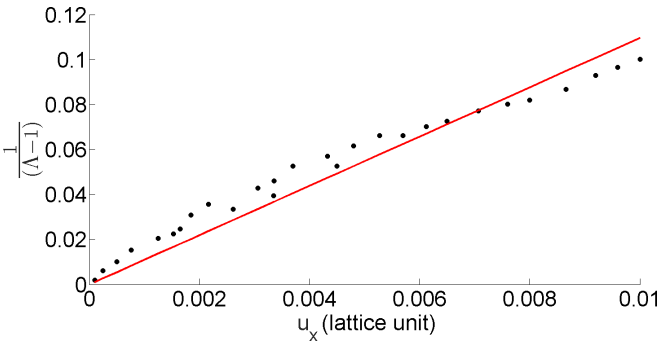

FIG. 7. A plot of density contrast Λ and the speed u at which a flat interface develops an error of 5%, according to Eq. (58). These data support the prediction of Eq. (49). The optimum straight line fit (solid line) was contained to intersect the origin.

VI. CONCLUSIONS

Continuum scale flows containing rapidly adjusting interfaces between completely immiscible fluid components, or phases, at significant density and viscosity contrast represent an important class of problems. Multicomponent lattice Boltzmann (MCLB) equation simulation is one of the small number of techniques able efficiently to address this regime. Of the several MCLB variants in current use (see Refs. [1,4,8,9,13] and the references therein), the chromodynamic variant, considered here, ignores questions of thermodynamic consistency. So, when a flow lies within the isothermal regime (i.e., is defined by mechanical considerations alone), it represents a useful, minimal tool [10]. In this regime, the utility of a chromodynamic MCLB has been demonstrated by Wen *et al.* [19] and Ba *et al.* [20], who advanced earlier work by Liu *et al.* [21]. This article adds theoretical support to the chromodynamic methodology of these authors by demonstrating that its kinematics is largely consistent with continuum scale requirements—here, we have demonstrated that color is a material invariant (which some may regard as an unsurprising relief). This outcome is achieved by analysis of the kinetic scale segregation rule [Eq. (10) above], which is usually neglected in the system dynamics. In terms of its mechanical properties (only), the result brings large density difference chromodynamic MCLB into line with other schemes, i.e., that of Inamuro *et al.* [11] and the free-energy variant [8]. The latter schemes, in contradistinction to the chromodynamic variant and perhaps wisely, postulate appropriate kinematics *a priori* and, in the case of the free-energy variant, reference a wider range of physics in their construction. That said, the analytical results in Sec. V confirm that, at the kinetic scale, for a range of density contrast, the emergent interface structure for a chromodynamic variant is isotropic, Galilean-invariant and it cannot diffuse. Accordingly, diffusion may not be added to the model in an attempt to enhance the limits of stability we see here. Here again, MCLB variants which contain an order parameter [8,11] (the analog of our color), with convection diffusion specified *a priori* have a possible advantage. Elsewhere, it seems unlikely that the practical density contrast achievable with the chromodynamic will reach that obtained using a Shan-Chen MCLB variant [9].

In more specific detail, our numerical data suggest that reported restrictions on the achievable density contrast in rapid flow, using chromodynamic MCLB, originate in the effect on the model's kinematics, of the terms deriving from the term F_{1i} we introduce below [Eq. (19)] in the evolution equation (24), which correct its dynamics, for large density differences. To remove the restrictions, one must better control the coupling between the dynamics and kinematics. Our analysis suggests that it would be difficult to devise an alternate segregation from Eq. (10) which retains those analytic properties shown here to be the key to appropriate continuum-scale kinematics. One approach may be to apply correction F_{1i} [see Eq. (39)] with a set of link weights, such that the essential correction to

the dynamics is preserved but the terms in s_e and s_v in Eq. (15) vanish.

APPENDIX A: ONE-DIMENSIONAL STATIC INTERFACE PROFILE

In this Appendix, we systematically derive the red and blue fluids' distribution close to the interface for a simplified one-dimensional static case when there is a density contrast between the fluids. We will be able to generalize our solution to find the general, unsteady, three-dimensional solution for the idealized case of correction terms F_{1i} negligible.

From Eqs. (22) and (42) and using $c_s^2 = \frac{1}{3}$ for D2Q9, we obtain

$$\begin{aligned} 0 = &\frac{3}{10}(1-\alpha_R)\delta_t^2 \frac{d^2}{dx^2}\left(\frac{\rho_R^2(x)}{\rho(x)}\right) \\ &+ \frac{3}{10}(1-\alpha_B)\delta_t^2 \frac{d^2}{dx^2}\left(\frac{\rho_R(x)\rho_B(x)}{\rho(x)}\right) \\ &- \frac{3}{5}\beta(1-\alpha_R)\delta_t^2 \frac{d}{dx}\left(\frac{\rho_R^2(x)\rho_B(x)}{\rho^2(x)}\right) \\ &- \frac{3}{5}\beta(1-\alpha_B)\delta_t^2 \frac{d}{dx}\left(\frac{\rho_R(x)\rho_B^2(x)}{\rho^2(x)}\right). \end{aligned} \tag{A1}$$

Taking a first integral to both sides of the above equation gives:

$$\begin{aligned} D_1 = &\frac{3}{10}(1-\alpha_R)\delta_t^2 \frac{d}{dx}\left(\frac{\rho_R^2(x)}{\rho(x)}\right) \\ &+ \frac{3}{10}(1-\alpha_B)\delta_t^2 \frac{d}{dx}\left(\frac{\rho_R(x)\rho_B(x)}{\rho(x)}\right) \\ &- \frac{3}{5}\beta(1-\alpha_R)\delta_t^2 \frac{\rho_R^2(x)\rho_B(x)}{\rho^2(x)} \\ &- \frac{3}{5}\beta(1-\alpha_B)\delta_t^2 \frac{\rho_R(x)\rho_B^2(x)}{\rho^2(x)}, \end{aligned} \tag{A2}$$

where D_1 is an unknown constant. When applying the boundary conditions, the integration constant D_1 can be determined to be zero from the following requirements:

$$\lim_{x\to\infty}(\rho_R(x)) = \rho_{0R}, \quad \lim_{x\to\infty}(\rho_B(x)) = 0, \tag{A3}$$

$$\lim_{x\to-\infty}(\rho_R(x)) = 0, \quad \lim_{x\to-\infty}(\rho_B(x)) = \rho_{0B}. \tag{A4}$$

Next we consider the symmetry of this one-dimensional problem. Exchanging the red fluid and blue fluids and replacing $\beta \to -\beta$, we obtain

$$\begin{aligned} D_2 = &\frac{3}{10}(1-\alpha_B)\delta_t^2 \frac{d}{dx}\left(\frac{\rho_B^2(x)}{\rho(x)}\right) \\ &+ \frac{3}{10}(1-\alpha_R)\delta_t^2 \frac{d}{dx}\left(\frac{\rho_R(x)\rho_B(x)}{\rho(x)}\right) \\ &+ \frac{3}{5}\beta(1-\alpha_B)\delta_t^2 \frac{\rho_R(x)\rho_B^2(x)}{\rho^2(x)} \\ &+ \frac{3}{5}\beta(1-\alpha_R)\delta_t^2 \frac{\rho_R^2(x)\rho_B(x)}{\rho^2(x)}, \end{aligned} \tag{A5}$$

where D_2 is another constant which can also be determined to be zero from boundary conditions in Eqs. (A3) and (A4). Summing Eqs. (A2) and (A5) and multiplying both sides of the new equation by $\frac{10}{3}$ leads to

$$\begin{aligned} 0 = &(1-\alpha_R)\delta_t^2 \frac{d}{dx}\left(\frac{\rho_R^2(x)+\rho_R(x)\rho_B(x)}{\rho(x)}\right) \\ &+ (1-\alpha_B)\delta_t^2 \frac{d}{dx}\left(\frac{\rho_B^2(x)+\rho_R(x)\rho_B(x)}{\rho(x)}\right). \end{aligned} \tag{A6}$$

Because $\rho_R(x) + \rho_B(x) = \rho(x)$, Eq. (A6) can be simplified to

$$(1-\alpha_R)\frac{d\rho_R(x)}{dx} + (1-\alpha_B)\frac{d\rho_B(x)}{dx} = 0. \tag{A7}$$

Integrating Eq. (A7) and performing simple algebraic manipulation leads to

$$\rho_R(x) + \Lambda\rho_B(x) = D_3, \tag{A8}$$

where $\Lambda = \frac{1-\alpha_B}{1-\alpha_R}$. Applying boundary conditions (A3) and (A4) again to determine that integration constant $D_3 = \rho_{0R}$, then we have, in summary:

$$\rho_B(x) = \frac{\rho_{0R} - \rho_R(x)}{\Lambda}, \tag{A9}$$

and

$$\rho(x) = \rho_R(x) + \rho_B(x) = \frac{\rho_{0R} + (\Lambda-1)\rho_R(x)}{\Lambda}. \tag{A10}$$

Now it is possible to return to Eq. (A2), using Eqs. (A9) and (A10) to reduce Eq. (A2) into a single unknown function; namely, $\rho_R(x)$, whereupon we obtain

$$\begin{aligned} 0 = &\frac{d}{dx}\left(\frac{\rho_R(x)}{(\Lambda-1)\rho_R(x)+\rho_{0R}}\right) \\ &- 2\beta\frac{\rho_R(x)[\rho_{0R}-\rho_R(x)]}{[(\Lambda-1)\rho_R(x)+\rho_{0R}]^2}. \end{aligned} \tag{A11}$$

Applying the product rule and the chain rule to Eq. (A11), we have

$$\begin{aligned} 0 = &\left(\frac{-\rho_{0R}(\Lambda-1)+(\Lambda-1)\rho_R(x)+\rho_{0R}}{[(\Lambda-1)\rho_R(x)+\rho_{0R}]^2}\right)\frac{d\rho_R(x)}{dx} \\ &- 2\beta\frac{\rho_R(x)[\rho_{0R}-\rho_R(x)]}{[(\Lambda-1)\rho_R(x)+\rho_{0R}]^2}, \end{aligned} \tag{A12}$$

which can be further simplified to

$$\frac{d}{dx}\rho_R(x) = \frac{2\beta\rho_R(x)[\rho_{0R}-\rho_R(x)]}{\rho_{0R}}, \tag{A13}$$

in which the variables may be separated:

$$\int \frac{1}{\rho_R[\rho_{0R}-\rho_R]}d\rho_R = \int \frac{2\beta}{\rho_{0R}}dx. \tag{A14}$$

The solution of Eq. (A14) is obtained by using partial fractions as

$$\rho_R(x) = \frac{\rho_{0R}}{1 + D_4\exp(-2\beta x)}, \tag{A15}$$

where D_4 is a constant to be determined. If the center of symmetry is placed at $x = 0$, D_4 can be determined to be 1.

Therefore, the solutions of red and blue fluids densities $\rho_R(x)$ and $\rho_B(x)$ are

$$\rho_R(x) = \frac{\rho_{0R}}{2}[1 + \tanh(\beta x)],$$
$$\rho_B(x) = \frac{\rho_{0B}}{2}[1 - \tanh(\beta x)]. \tag{A16}$$

APPENDIX B: KINEMATIC EQUATION FOR A MULTIRELAXATION-TIME SCHEME

The interplay between model kinematics and dynamics is more difficult to analyze for a chromodynamic method which is based upon a multiple relaxation time scheme (MRT). However, MRT schemes are known to be much more stable and accurate than their LBGK counterparts. The color gradient MCLB and segregation scheme analyzed here was originally devised by Ba. *et al.* who deployed it with a more stable MRT collision scheme [20]. The equilibrium of the MRT scheme of Ba. *et al.* is

$$f_i^{(0)}(\rho, \mathbf{u}) = \rho\phi_i + t_i\rho\left(\frac{u_\alpha c_{i\alpha}}{c_s^2}(1 + h_i) + \frac{u_\alpha u_\beta c_{i\alpha}c_{i\beta}}{2c_s^4} - \frac{u^2}{2c_s^2}\right),$$
$$h_i = \Gamma(\mathbf{r})(3c_{i\beta}c_{i\beta} - 4),$$
$$\Gamma(\mathbf{r}) = \frac{4\rho - 9(\alpha_R\rho_R + \alpha_B\rho_B)}{10\rho}, \tag{B1}$$

which, note, is more complex that our LBGK equivalent. This necessitates greater care in the derivation of its kinematics. The LDD correction and immersed boundary sources for Ba's MRT scheme are

$$F_{1i} = \frac{1}{12}\left[\left(1 - \frac{s_e}{2}\right)(4 - 3c_i^2)C_{B1} + 3(c_{ix}^2 - c_{iy}^2)\left(1 - \frac{s_v}{2}\right)C_{B7}\right],$$
$$F_{2i} = \left(1 - \frac{s_v}{2}\right)\left(\frac{(F_\alpha - u_\alpha)c_{i\alpha}}{c_s^2} + \frac{F_\alpha u_\beta c_{i\alpha}c_{i\beta}}{2c_s^4}\right), \tag{B2}$$

with the latter identical to our simpler LBGK scheme, note. Note also that two MRT relaxation scheme parameters now appear (see Ba *et al.* [20]) and

$$\phi_i = \begin{cases} \frac{\alpha_R\rho_R}{\rho} + \frac{\alpha_B\rho_B}{\rho}, & i = 0 \\ (1 - \alpha_R)\frac{s_i\rho_R}{\rho} + (1 - \alpha_B)\frac{s_i\rho_B}{\rho}, & i \neq 0, \end{cases} \tag{B3}$$

$$C_{B1} = \frac{9}{5}\partial_\alpha\left\{\left[(1 - \alpha_R)\rho_R + (1 - \alpha_B)\rho_B - \frac{5\rho}{9}\right]u_\alpha\right\}, \tag{B4}$$

$$C_{B7} = \frac{9}{5}\partial_\alpha\left\{\left[(1 - \alpha_R)\rho_R + (1 - \alpha_B)\rho_B - \frac{5\rho}{9}\right]u_\alpha\right\}. \tag{B5}$$

Following the analysis of Sec. III with the above modifications, we obtain, in place of Eq. (13),

$$\begin{aligned}\rho_R(\mathbf{r}, t + \delta_t) = &\sum_{\forall i}\rho_R\left[\phi_i + t_i\left(\frac{u_\alpha c_{i\alpha}}{c_s^2}(1 + h_i) + \frac{u_\alpha u_\beta c_{i\alpha}c_{i\beta}}{2c_s^4} - \frac{u^2}{2c_s^2}\right)\right]_{\mathbf{r}-\delta_t\mathbf{c}_i} \\ &+ \frac{1}{12}\sum_{\forall i}\frac{\rho_R}{\rho}\left[\left(1 - \frac{s_e}{2}\right)(4 - 3c_i^2)C_{B1}\right]_{\mathbf{r}-\delta_t\mathbf{c}_i} \\ &+ \frac{1}{4}\sum_{\forall i}\frac{\rho_R}{\rho}\left[\left(1 - \frac{s_v}{2}\right)(c_{ix}^2 - c_{iy}^2)C_{B7}\right]_{\mathbf{r}-\delta_t\mathbf{c}_i} \\ &+ \delta_t\beta\sum_{\forall i}\left[\phi_i\left(\frac{\rho_R\rho_B}{\rho}\right)n_\beta c_{i\beta}\right]_{\mathbf{r}-\delta_t\mathbf{c}_i}.\end{aligned} \tag{B6}$$

Performing the Taylor expansions, we obtain the following in place of Eq. (15):

$$\begin{aligned}\rho_R + \delta_t\frac{\partial\rho_R}{\partial t} + \frac{1}{2}\delta_t^2\frac{\partial^2\rho_R}{\partial t^2} = &(1 - \alpha_R)\sum_{i\neq 0}s_i\left[\frac{\rho_R^2}{\rho} - \delta_t c_{i\alpha}\partial_\alpha\left(\frac{\rho_R^2}{\rho}\right) + \frac{\delta_t^2}{2}c_{i\alpha}c_{i\beta}\partial_\alpha\partial_\beta\left(\frac{\rho_R^2}{\rho}\right)\right] \\ &+ (1 - \alpha_B)\sum_{i\neq 0}s_i\left[\frac{\rho_R\rho_B}{\rho} - \delta_t c_{i\alpha}\partial_\alpha\left(\frac{\rho_R\rho_B}{\rho}\right) + \frac{\delta_t^2}{2}c_{i\alpha}c_{i\beta}\partial_\alpha\partial_\beta\left(\frac{\rho_R\rho_B}{\rho}\right)\right] \\ &+ \frac{\alpha_R\rho_R^2}{\rho} + \frac{\alpha_B\rho_B\rho_R}{\rho} + \frac{u_\gamma}{c_s^2}\sum_{\forall i}t_i\left[\rho_R - \delta_t c_{i\alpha}\partial_\alpha\rho_R + \frac{\delta_t^2}{2}c_{i\alpha}c_{i\beta}\partial_\alpha\partial_\beta\rho_R\right]c_{i\gamma} \\ &+ \frac{u_\gamma}{c_s^2}\sum_{\forall i}t_i\left[\frac{\rho_R\Gamma}{\rho} - \delta_t c_{i\alpha}\partial_\alpha\left(\frac{\rho_R\Gamma}{\rho}\right) + \frac{\delta_t^2}{2}c_{i\alpha}c_{i\beta}\partial_\alpha\partial_\beta\left(\frac{\rho_R\Gamma}{\rho}\right)\right](3c_i^2 - 4)c_{i\gamma} \\ &+ \frac{u_\alpha u_\beta}{2c_s^4}\sum_{\forall i}t_i\left[\rho_R - \delta_t c_{i\gamma}\partial_\gamma\rho_R + \frac{\delta_t^2}{2}c_{i\gamma}c_{i\delta}\partial_\gamma\partial_\delta\rho_R\right]c_{i\alpha}c_{i\beta} \\ &- \frac{u^2}{2c_s^2}\sum_{\forall i}t_i\left[\rho_R - \delta_t c_{i\alpha}\partial_\alpha\rho_R + \frac{\delta_t^2}{2}c_{i\alpha}c_{i\beta}\partial_\alpha\partial_\beta\rho_R\right]\end{aligned}$$

$$
\begin{aligned}
&+\frac{1}{12}\left(1-\frac{s_e}{2}\right)\sum_{\forall\, i}\left[\frac{\rho_R C_{B1}}{\rho}-\delta_t c_{i\alpha}\partial_\alpha\left(\frac{\rho_R C_{B1}}{\rho}\right)+\frac{\delta_t^2}{2}c_{i\alpha}c_{i\beta}\partial_\alpha\partial_\beta\left(\frac{\rho_R C_{B1}}{\rho}\right)\right]\left(4-3c_i^2\right)\\
&+\frac{1}{4}\left(1-\frac{s_v}{2}\right)\sum_{\forall\, i}\left[\frac{\rho_R C_{B7}}{\rho}-\delta_t c_{i\alpha}\partial_\alpha\left(\frac{\rho_R C_{B7}}{\rho}\right)+\frac{\delta_t^2}{2}c_{i\alpha}c_{i\beta}\partial_\alpha\partial_\beta\left(\frac{\rho_R C_{B7}}{\rho}\right)\right]\left(c_{ix}^2-c_{iy}^2\right)\\
&+\delta_t\beta(1-\alpha_R)\sum_{i\neq 0}s_i\left[\frac{\rho_R^2\rho_B}{\rho^2}-\delta_t c_{i\alpha}\partial_\alpha\left(\frac{\rho_R^2\rho_B}{\rho^2}\right)+\frac{\delta_t^2}{2}c_{i\alpha}c_{i\beta}\partial_\alpha\partial_\beta\left(\frac{\rho_R^2\rho_B}{\rho^2}\right)\right]n_\gamma c_{i\gamma}\\
&+\delta_t\beta(1-\alpha_B)\sum_{i\neq 0}s_i\left[\frac{\rho_R\rho_B^2}{\rho^2}-\delta_t c_{i\alpha}\partial_\alpha\left(\frac{\rho_R\rho_B^2}{\rho^2}\right)+\frac{\delta_t^2}{2}c_{i\alpha}c_{i\beta}\partial_\alpha\partial_\beta\left(\frac{\rho_R\rho_B^2}{\rho^2}\right)\right]n_\gamma c_{i\gamma},
\end{aligned}
\tag{B7}
$$

in which, note, the influence of the collision model appears in several terms. Again assuming lattice isotropy properties, using our previous definition of the s_i and k we can simplify to

$$
\begin{aligned}
\delta_t\frac{\partial\rho_R}{\partial t}+\frac{1}{2}\delta_t^2\frac{\partial^2\rho_R}{\partial t^2}+\delta_t u_\gamma\partial_\gamma\rho_R=&\frac{k}{2}c_s^2(1-\alpha_R)\delta_t^2\nabla^2\left(\frac{\rho_R^2}{\rho}\right)+\frac{k}{2}c_s^2(1-\alpha_B)\delta_t^2\nabla^2\left(\frac{\rho_R\rho_B}{\rho}\right)\\
&+\frac{1}{2}\delta_t^2u_\alpha u_\beta\partial_\alpha\partial_\beta\rho_R-\delta_t^2\beta(1-\alpha_R)kc_s^2n_\gamma\partial_\gamma\left(\frac{\rho_R^2\rho_B}{\rho^2}\right)\\
&-\delta_t^2\beta(1-\alpha_B)kc_s^2n_\gamma\partial_\gamma\left(\frac{\rho_R\rho_B^2}{\rho^2}\right)+\frac{1}{12}\delta_t^2\left(1-\frac{s_e}{2}\right)\nabla^2\left(\frac{\rho_R C_{B1}}{\rho}\right)\\
&+\frac{1}{4}\delta_t^2\left(1-\frac{s_v}{2}\right)\left(\partial_x^2-\partial_y^2\right)\left(\frac{\rho_R C_{B7}}{\rho}\right).
\end{aligned}
\tag{B8}
$$

Note that all terms containing the quantity Γ have vanished between Eqs. (B7) and (B8). However, relaxation-parameter-dependent terms originating in the dynamics' density correction term F_{1i} remain. These terms may be transformed by using the identities in Eqs. (B4) and (B5):

$$
\begin{aligned}
\delta_t\frac{\partial\rho_R}{\partial t}+\frac{1}{2}\delta_t^2\frac{\partial^2\rho_R}{\partial t^2}+\delta_t u_\gamma\partial_\gamma\rho_R=&\frac{k}{2}c_s^2(1-\alpha_R)\delta_t^2\nabla^2\left(\frac{\rho_R^2}{\rho}\right)+\frac{k}{2}c_s^2(1-\alpha_B)\delta_t^2\nabla^2\left(\frac{\rho_R\rho_B}{\rho}\right)\\
&+\frac{1}{2}\delta_t^2u_\alpha u_\beta\partial_\alpha\partial_\beta\rho_R-\delta_t^2\beta(1-\alpha_R)kc_s^2n_\gamma\partial_\gamma\left(\frac{\rho_R^2\rho_B}{\rho^2}\right)\\
&-\delta_t^2\beta(1-\alpha_B)kc_s^2n_\gamma\partial_\gamma\left(\frac{\rho_R\rho_B^2}{\rho^2}\right)+\frac{k\delta_t^2}{12}(1-\alpha_R)\left(1-\frac{s_e}{2}\right)u_\alpha\partial_\alpha\nabla^2\left(\frac{\rho_R^2}{\rho}\right)\\
&+\frac{k\delta_t^2}{12}(1-\alpha_B)\left(1-\frac{s_e}{2}\right)u_\alpha\partial_\alpha\nabla^2\left(\frac{\rho_R\rho_B}{\rho}\right)-\frac{\delta_t^2}{12k}\left(1-\frac{s_e}{2}\right)u_\alpha\partial_\alpha\nabla^2\rho\\
&+\frac{5k\delta_t^2}{36}(1-\alpha_R)\left(1-\frac{s_v}{2}\right)\epsilon_{z\alpha\beta}u_\alpha\partial_\beta\left(\partial_x^2-\partial_y^2\right)\left(\frac{\rho_R^2}{\rho}\right)\\
&+\frac{5k\delta_t^2}{36}(1-\alpha_B)\left(1-\frac{s_v}{2}\right)\epsilon_{z\alpha\beta}u_\alpha\partial_\beta\left(\partial_x^2-\partial_y^2\right)\left(\frac{\rho_R\rho_B}{\rho}\right)\\
&-\frac{\delta_t^2}{4k}\left(1-\frac{s_v}{2}\right)\epsilon_{z\alpha\beta}u_\alpha\partial_\beta\left(\partial_x^2-\partial_y^2\right)\rho.
\end{aligned}
\tag{B9}
$$

Here, $\epsilon_{z\alpha\beta}$ is the unit antisymmetric tensor.

[1] A. K. Gunstensen, D. H. Rothman, S. Zaleski, and G. Zanetti, Phys. Rev. A **43**, 4320 (1991).

[2] D. H. Rothman and J. M. Keller, J. Stat. Phys. **52**, 1119 (1988).

[3] D. H. Rothman and S. Zaleski, *Lattice-Gas Cellular Automata: Simple Models of Complex Hydrodynamics* (Cambridge University Press, 2004).

[4] M. R. Swift, W. R. Osborn, and J. M. Yeomans, Phys. Rev. Lett. **75**, 830 (1995).

[5] M. R. Swift, E. Orlandini, W. R. Osborn, and J. M. Yeomans, Phys. Rev. E **54**, 5041 (1996).

[6] A. J. Wagner, Phys. Rev. E **74**, 056703 (2006).

[7] Q. Li and A. J. Wagner, Phys. Rev. E **76**, 036701 (2007), and references therein.

[8] A. J. Wagner and C. M. Pooley, Phys. Rev. E **76**, 045702(R) (2007), and references therein.
[9] X. Shan and H. Chen, Phys. Rev. E **49**, 2941 (1994).
[10] J. Yang and E. S. Boek, Comput. Math. Appl. **65**, 882 (2013).
[11] T. Inamuro, T. Ogata, S. Tajima, and N. Konishi, J. Comput. Phys. **198**, 628 (2004).
[12] L. Landau and E. M. Lifshitz, *Fluid Mechanics* (Pergamon Press, Oxford, 1959), 1st ed.
[13] S. V. Lishchuk, C. M. Care, and I. Halliday, Phys. Rev. E **67**, 036701(2) (2003).
[14] U. D'Ortona, D. Salin, M. Cieplak, R. B. Rybka, and J. R. Banavar, Phys. Rev. E **51**, 3718 (1995).
[15] C. S. Peskin, Acta Numerica **11**, 479 (2002).
[16] Z. Guo, C. Zheng, and B. Shi, Phys. Rev. E **65**, 046308 (2002).
[17] I. Halliday, A. P. Hollis, and C. M. Care, Phys. Rev. E **76**, 026708 (2007).
[18] T. Reiss and T. N. Phillips, J. Phys. A: Math. Theor. **40**, 4033 (2007).
[19] Z. X. Wen, Q. Li, Y. Yu, and Kai H. Luo, Phys. Rev. E **100**, 023301 (2019).
[20] Y. Ba, H. Liu, Q. Li, Q. Kang, and J. Sun, Phys. Rev. E **94**, 023310 (2016).
[21] H. Liu, A. J. Valocchi, and Q. Kang, Phys. Rev. E **85**, 046309 (2012).
[22] Y. H. Qian, D. d'Humières, and P. Lallemand, Europhys. Lett. **17**, 479 (1992).
[23] S. Hou, Q. Zou, S. Chen, G. Doolen, and A. C. Cogley, J. Comput. Phys. **118**, 329 (1995).
[24] P. Lallemand and L.-S. Luo, Phys. Rev. E **61**, 6546 (2000).
[25] I. Halliday, X. Xu, and K. Burgin, Phys. Rev. E **95**, 023301 (2017).
[26] X. Xu, K. Burgin, M. A. Ellis, and I. Halliday, Phys. Rev. E **96**, 053308 (2017).
[27] I. Halliday, S. V. Lishchuk, T. J. Spencer, K. Burgin, and T. Schenkel, Comput. Phys. Commun. **219**, 286 (2017).
[28] T. J. Spencer and I. Halliday, Phys. Rev. E **88**, 063305 (2013).